Diploma Thesis

Comparison and Connection of the Similarity Renormalization Group and the Unitary Correlation Operator Method

Sabine Reinhardt

TU Darmstadt

2008

Contents

Introduction

A major challenge in theoretical nuclear physics is to find a way to describe the properties of an atomic nucleus based on the interaction of the constituent nucleons. This poses several difficulties, since the interaction between the nucleons has a very complex structure and the quantum mechanical many-body problem cannot be solved analytically.
The strong interaction that describes the nuclear interaction is based on Quantum Chromodynamics. Thus it seems to be obvious to extract the interaction from this theory, but this is not feasible (yet) because the theory is non-perturbative in the low-energy regime relevant of nuclear physics. Nuclear interactions are therefore constructed such that they contain the low-energy physics and symmetries of Quantum Chromodynamics. This approach leaves some parameters of the resulting interactions undetermined, which are fit to experimental data. There exist several of these interactions: one group, the traditional realistic potentials consists of a phenomenological part and a meson exchange part; another group, the so-called chiral potentials, is based on chiral effective field theory. For applications beyond nucleon-nucleon scattering and the calculation of deuteron properties, the chiral effective field theory gives a set of consistent many-nucleon forces.
In the first chapter one potential of each of these groups, the realistic potential Argonne V18 [1] and the chiral potential at next-to-next-to-next-to leading order (N3LO) [2], will be discussed, as they will be used for further calculations. For the solution of the quantum mechanical many-body problem several approaches exist. For light nuclei, quasi-exact numerical methods like the No-Core Shell Model (NCSM) can be used. For heavier nuclei these methods would exceed the computational resources. Therefore, appropriate approximations are needed. A starting point for first estimations is the self-consistent Hartree-Fock method, where all interactions to one nucleon are replaced with an average interaction. In that case the Hilbert space is restricted to a one-dimensional model space that provides simplifications within the calculations. The problem that occurs within this description are strong correlations created by the nucleon-nucleon interaction. These correlations are generated by the repulsion at small nucleon-nucleon distances and by the tensor part of the interaction. To properly describe these effects, the Unitary Correlation Operator Method (UCOM) [3, 4, 5, 6] was introduced, where the short-range correlations are treated by unitary transformations. Two unitary correlation operators are introduced, one for the

central correlations and one for the tensor correlations. Within this method the nuclear interaction is transformed into an effective interaction that is well suited for simple model spaces. In the second chapter the properties of the UCOM and the generation of the correlated interaction will be discussed.
Another method to construct an effective interaction is the Similarity Renormalization Group (SRG) [7, 8, 9, 10] which will be introduced in the third chapter. The basic idea of this method is to transform the many-body Hamiltonian of the system to a band-diagonal structure in an appropriate basis. The pre-diagonalization is performed by evolving a unitarily transformed Hamiltonian within a flow equation. In Chapter four this method will be compared to the UCOM and their connection will be discussed. The SRG provides a new conceptual approach to the construction of UCOM correlation functions, which will be applied to the Argonne V18 and chiral N3LO interactions. The structure of these correlation functions will be compared to the correlation functions obtained with the previous variational approach discussed in [11].
The new effective interactions are then used as input for the nuclear many-body problem. In the fifth chapter results of NCSM calculations are discussed for the Argonne V18 potential. Results for effective interactions obtained with the SRG approach, the variationally optimized UCOM, and the SRG-optimized UCOM transformations will be compared. The Hartree-Fock method [12, 13] that is based on the variational principle gives first trends of the ground state properties of the atomic nucleus. With this method the properties of a number of nuclei, ranging from ^{4}He to ^{208}Pb, will be examined in the sixth chapter. A summary will be given in Chapter seven.

Chapter 1

Realistic Nucleon-Nucleon Potentials

1.1 Historical Overview

Until James Chadwick discovered the neutron in 1932 [14] the atomic nucleus was assumed to consist of protons and electrons. This new particle inspired Werner Heisenberg and independently Dmitri Iwanenko [15] to conclude that the nucleus consists of protons and neutrons and does not contain any electrons. This new model immediately raised the question about a nuclear force that is responsible for the binding of nuclei.
A first ansatz for such a nuclear force was made by Hideki Yukawa in 1935 [16] with his meson theory, a field theoretic attempt to derive the interaction from meson exchange. In this model the nucleons interact via the exchange of mesons. The pion, discovered in 1947, was considered to be the carrier of the nuclear force, analogous to the photon in quantum electrodynamics. The one-pion exchange turned out to describe the experimental nucleon-nucleon scattering data very well at low energies, while the two-pion exchange alone does not fit experimental data at intermediate energies at all. Later the multi-pion theories were considered a failure, since the significant effect of chiral symmetry on pion dynamics was not known at that time.
With the first quark-model by Murray Gell-Mann in 1964, new attempts to describe the nucleon-nucleon interaction were made. Quantum Chromodynamics (QCD) describes the substructure of the nucleons, the quarks and gluons. In this theory the nucleons consist of quarks that are attracted by a force that is induced by the exchange of gluons. QCD is a relativistic quantum field theory with some unpleasant properties. A major problem of QCD is its non-perturbative character at low energies, hence perturbation theory cannot be used for describing the structure of nucleons. Describing the nuclear force in terms of quarks and gluons is a very complicated problem, since the force binding nucleons together is of residual character [2].

Nucleon-nucleon potentials have to satisfy the symmetries of QCD, as for example Galilei invariance, translation invariance and parity invariance [12]. Anyhow there remain some parameters which cannot be obtained by theoretical arguments. These parameters are fitted to experimental data like nucleon-nucleon scattering phase shifts. Potentials that reproduce the experimental nucleon-nucleon scattering data and deuteron properties are called realistic potentials.
In the 1990s chiral Effective Field Theory (χEFT) was introduced and applied to QCD in the low energy regime. This new theory provides the possibility to describe the nucleon-nucleon interaction in terms of pions and nucleons rather than quarks and gluons.
In this thesis two different nucleon-nucleon potentials are used, the realistic potential Argonne V18 (Section 1.2) and the chiral N3LO potential (Section 1.3).

1.2 Argonne V18 Potential

Realistic nucleon-nucleon interactions consist of a short-range repulsion for particle distances up to $\simeq 0.5\,\mathrm{fm}$ and an attractive part for distances of $1 - 2\,\mathrm{fm}$. There is also a spin-orbit part in the interaction and a tensor part that depends on the orientation of the spins of the interacting particles.
One of these realistic potentials is the Argonne V18 potential. It consists of three main parts, a long-range part that is due to one-pion exchange, a medium- and short-range part consisting of phenomenological parametrizations, and a third part describing the electromagnetic interaction [1].
The phenomenological part

$$V_{ST} = V_{ST}^{c}(r) + V_{ST}^{t}(r)\, S_{12}(\boldsymbol{r},\boldsymbol{r}) + V_{ST}^{ls}(r)\, \boldsymbol{L}\cdot\boldsymbol{S} + V_{ST}^{ls2}(r)\, (\boldsymbol{L}\cdot\boldsymbol{S})^2 + V_{ST}^{l2}(r)\, \boldsymbol{L}^2 \qquad (1.1)$$

contains a central $V_{ST}^{c}(r)$, a tensor $V_{ST}^{t}(r)$, a spin-orbit $V_{ST}^{ls}(r)$, a quadratic spin-orbit $V_{ST}^{ls2}(r)$ and a quadratic angular momentum $V_{ST}^{l2}(r)$ component. Here

$$S_{12}(\boldsymbol{r},\boldsymbol{r}) = \frac{3}{r^2}\,(\boldsymbol{\sigma}_1\cdot\boldsymbol{r})\,(\boldsymbol{\sigma}_2\cdot\boldsymbol{r}) - \boldsymbol{\sigma}_1\cdot\boldsymbol{\sigma}_2 \qquad (1.2)$$

is the tensor operator and $\boldsymbol{\sigma}_n$ is the spin of the nth particle. Each of these parts is given in the general form

$$V_{ST}^{i}(r) = I_{ST}^{i}\, T_{\mu}^{2}(r) + \left[P_{ST}^{i} + \mu\, r\, Q_{ST}^{i} + (\mu\, r)^2\, R_{ST}^{i}\right] W(r). \qquad (1.3)$$

$W(r)$ is the Woods-Saxon function providing the short-range core, $\mu = \frac{1}{3}\,(m_{\pi^0} + 2\,m_{\pi^\pm})$ is the average pion mass, and $T_{\mu}(r)$ are Yukawa functions multiplied with exponential form factors $(1-\mathrm{e}^{-c\,r^2})$ and $(1-\mathrm{e}^{-c\,r^2})^2$. The parameters I_{ST}^{i}, P_{ST}^{i}, Q_{ST}^{i} and R_{ST}^{i} which describe the radial dependence of each $V_{ST}^{i}(r)$ are undetermined and have to be fit to data.

In general potentials are fitted to *pp* or *np* scattering data to obtain these parameters, but unfortunately potentials fitted to *pp* data give a mediocre description of *np* results and vice versa. This is due to charge independence breaking in the strong interaction, even after introducing the necessary corrections for the Coulomb interaction. Charge-independence breaking means, that for isospin $T = 1$ the *pp*, *np* and *nn* interactions are different after electromagnetic effects have been removed. The Argonne V18 potential therefore explicitly takes charge-independence breaking into account for the fit of *np* and *pp* data as well as low-energy *nn* data and deuteron properties. The general form of the potential is given by

$$V_{ST} = \sum_p V_p^{ST}(r)\, O_p \tag{1.4}$$

with 18 operators O_p, 14 of them are charge independent. This means that there is no differentiation between *pp*, *nn* or *np* interactions. There are also a charge-dependent and a charge-asymmetric part improving the agreement of *pp* and *np* scattering data.
Typically nuclei are underbound when using nucleon-nucleon potentials fit to scattering data [1]. Many-nucleon interactions are expected to be responsible for a part of this missing binding energy. Therefore, a three-nucleon potential is necessary for a correct description. This correction is not included in the Argonne V18 potential, but there are phenomenological three-nucleon potentials consisting of the Argonne V18 potential and the three-nucleon interaction of the Urbana IX model (see [17]).

1.3 Chiral Potentials

Effective field theories (EFTs) are low-energy approximations to more fundamental quantum field theories. This is reasonable, since many physical effects can be explained without resolving the substructure of the system, which comes into play for higher energies.
To derive a nuclear force from QCD the EFT-concept can be used. The relevant degrees of freedom have to be identified and it has to be ensured that the symmetries of QCD are fulfilled. Weinberg showed that the most general Lagrangian consistent with the symmetries of the underlying theory has to be considered to construct an EFT. It yields the most general possible S-matrix that is consistent with these symmetries, analyticity, perturbative unitarity and the cluster decomposition principle [18].
The spontaneous breaking of chiral symmetry causes the transition from the *fundamental* QCD to an EFT. Spontaneous symmetry breaking means that the ground state does not respect a particular symmetry of the Lagrangian. For chiral symmetry between the up and the down quark, an SU(2) isospin symmetry is observed, while the axial symmetry is broken in the QCD ground state. This breakdown implies the existence of Goldstone bosons with the quantum numbers of the broken generators. The Goldstone bosons can be identified by the three pions, π^0 and $\pi^\pm$ [19].

The relevant degrees of freedom for describing the nuclear force are nucleons and pions. Since the interaction of Goldstone bosons vanishes at zero momentum transfer and in the chiral limit at vanishing quark masses $m \to 0$, the low-energy expansion of the Lagrangian is arranged in powers of derivatives and pion masses. This is known as the chiral perturbation theory (χPT) [20]. The interaction terms of the Lagrangian are classified by powers of $(p/\Lambda_\chi)^\nu$, where p is the pion four-momentum and Λ_χ is the chiral symmetry breaking scale up to which the effective theory is valid. The determination of the power ν is known as power counting [2].

χPT is applied up to the scale Λ_χ which is usually considered as the mass of the ρ-meson, since the ρ is the lightest meson ($m_\rho \approx 770\text{MeV/c}^2$) that cannot be identified as a Goldstone boson from the breaking of chiral symmetry.

Since the mass of the nucleons is not small compared to Λ_χ, the treatment of a system of two nucleons in χPT is not simple. To resolve this issue, the Lagrangian is expanded in terms of powers of $1/m_N$. This method is known as the heavy baryon formulation of χPT. Within this framework the effective Lagrangian, which is used for deriving a nuclear force, can be set up. The Lagrangian consists of terms describing the interaction between two pions and of terms dealing with pion-nucleon interactions. The expansion within χPT leads to a series of interaction terms containing derivatives of the Lagrangian. Expanding to next-to-next-to-next-to leading order (N3LO) generates one pion exchange, two pion exchange and three pion exchange, where the effect of three pion exchange turns out to be negligible [21]. One advantage of χPT is, that it also generates many-nucleon forces during the expansion. In χPT at N3LO also three and four nucleon forces are included. The three nucleon force is very involved in that order, the contribution of the four nucleon force in contrast is very small. Nevertheless the existence of many-nucleon forces is an important result especially in comparison to other potentials, for example the Argonne V18 which was optimized to two nucleon forces.

The nucleon-nucleon potential is calculated by using perturbation theory and application of the results to a scattering equation. The full chiral nucleon-nucleon potential consists of pion exchange V_π and contact terms V_{ct}, $V = V_\pi + V_{\text{ct}}$. Since charge dependence is important for an accurate description of low-energy pp and np data, it is included in the potential, as well as the pion mass difference and the Coulomb potential [2].

Figure 1.1 shows the deuteron wavefunctions derived from the two N3LO potentials, namely Jülich and Idaho in comparison to the wavefunctions obtained from the Argonne V18, CD Bonn and Nijmegen-I potentials. The chiral wavefunctions are shifted towards a larger r. One interesting property of the chiral wavefunctions is the oscillation for larger r in the D-wave for the Idaho potential and in the S-wave in the case of the Jülich potential. This effect will show up again in Chapter 4, where it will cause some difficulties. In the following it will always be referred to the Idaho N3LO potential.

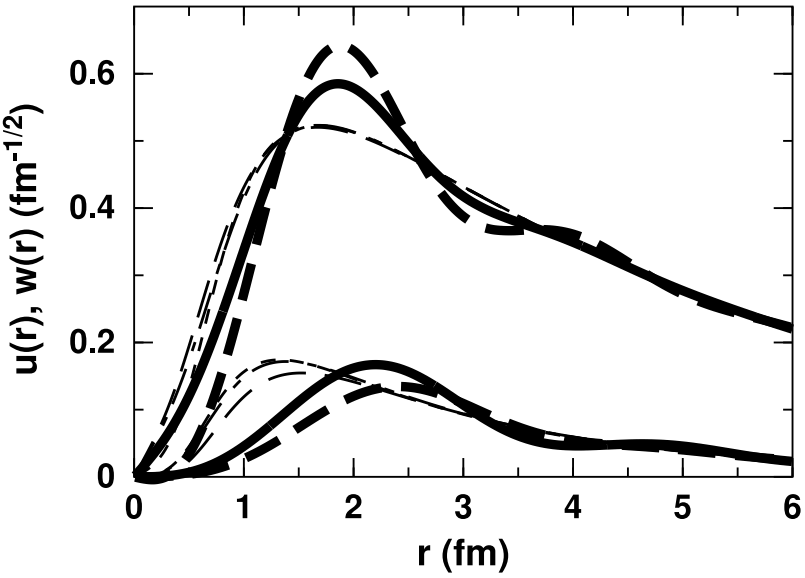

Figure 1.1: The deuteron wavefunction with the S-wave (upper curves) and the D-wave (lower curves) components is shown. The thick lines represent chiral N3LO potentials (solid: Idaho, dashed: Jülich). The thin lines refer to the Argonne V18 potential (dotted), the CD Bonn potential (solid) and the Nijmegen-I potential (dash-dotted), (from [2]).

Chapter 2

The Unitary Correlation Operator Method

2.1 Basic Concepts

The invention of realistic nucleon-nucleon potentials in principle allows for the description of atomic nuclei within *ab initio* methods that need no further approximations. These methods are restricted to light nuclei by computational resources. For heavier nuclei approximations are required, staying as close as possible to the *ab initio* treatment. The simplest possible many-body states are the single Slater determinants as used in Hartree-Fock (see Chapter 6). The problem with the Hartree-Fock approach is that correlations, like those induced by realistic nucleon-nucleon interactions, cannot be described with one Slater determinant. To resolve this, the correlations are introduced into the many-body states by means of unitary correlation operators. Unitary operators are chosen since they preserve the norm of the state they are applied to.
In this thesis two different methods for handling the short-range properties of realistic nucleon-nucleon interactions by means of unitary transformations are employed. One is the Similarity Renormalization Group (SRG), which will be discussed in Chapter 3, the other is the Unitary Correlation Operator Method (UCOM) [3, 4, 5, 6] which will be explained in the following.
In the UCOM transformation

$$|\tilde{\Psi}\rangle = C\,|\Psi\rangle, \tag{2.1}$$

the unitary correlation operator C acts on an uncorrelated initial state $|\Psi\rangle$ and a new correlated state $|\tilde{\Psi}\rangle$ results. Due to the unitarity of the correlation operator it can alternatively be applied to an operator O, leading to a correlated operator $\tilde{O}$:

$$\langle\tilde{\Psi}'|O|\tilde{\Psi}\rangle = \langle\Psi'|C^\dagger OC|\Psi\rangle = \langle\Psi'|\tilde{O}|\Psi\rangle. \tag{2.2}$$

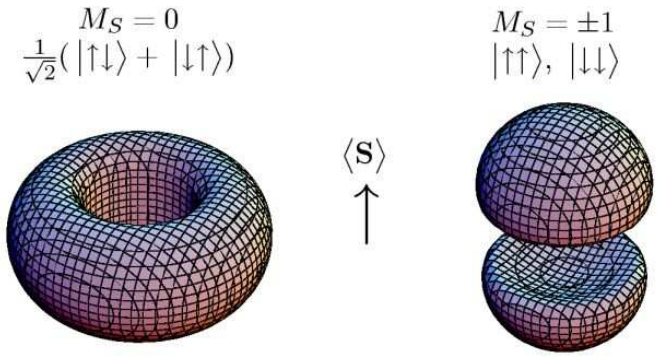

Figure 2.1: Two-body density distribution of the deuteron calculated with the Argonne V18 potential. The isodensity surface for $0.005\,\mathrm{fm}^{-3}$ is shown, (from [23]).

The structure of the correlations already appears in the deuteron [22, 23, 4, 6]. In Figure 2.1 the spin-projected two-body density distribution of the deuteron is displayed. On the left of the figure the magnetic spin quantum number is $M_S = 0$, the spins are aligned anti-parallel. The right-hand part of the figure shows parallel spins, $M_S = \pm 1$. For small particle distances, the probability of finding two nucleons very close to each other is nearly zero, since the short-range repulsion in the central interaction pushes them apart. The tensor correlations are spin-dependent. The probability density for anti-parallel spins is concentrated in a *torus*, while for parallel spins a *dumbbell* is favored. This figure shows that the central and the tensor correlations play an important role for describing the properties of a nucleus. Therefore they are treated explicitly with the central correlation operator C_r and the tensor correlation operator C_Ω [23]:

$$C = C_\Omega \, C_r. \tag{2.3}$$

The central correlation operator accounts for the effects of the short-range repulsion of the interaction (the core), the tensor correlation operator represents the short-range part of the tensor interaction. The correlation operators are unitary, therefore they can be written as exponential functions of hermitian generators G_Ω and G_r [23]

$$C_\Omega \, C_r = \mathrm{e}^{-\mathrm{i}\, G_\Omega} \, \mathrm{e}^{-\mathrm{i}\, G_r} = \exp\left[-\mathrm{i} \sum_{i<j} g_{\Omega,ij}\right] \, \exp\left[-\mathrm{i} \sum_{i<j} g_{r,ij}\right]. \tag{2.4}$$

Here the generators g_r for the central correlation operator and g_Ω for the tensor correlation operator are assumed to be two-body operators, since they result from a two-body interaction. Their structure is motivated by the form of the correlations, as shown in Section 2.2 for g_r and in Section 2.3 for g_Ω.

2.2 Central Correlations

The central correlation operator has to be constructed such that it has a large impact on the nucleons if their distance is small and does not act if their distance is larger than the core radius. For central correlations the generator

$$g_r = \frac{1}{2}\left[s(r)\, q_r + q_r\, s(r)\right]\, \Pi_{ST} \tag{2.5}$$

causes distance dependent radial shifts with the projection operator Π_{ST} onto spin S and isospin T. Here

$$q_r = \frac{1}{2}\left[\frac{\boldsymbol{r}}{r}\cdot\boldsymbol{q} + \boldsymbol{q}\cdot\frac{\boldsymbol{r}}{r}\right] \tag{2.6}$$

is the radial component of the relative momentum $\boldsymbol{q} = \frac{1}{2}[\boldsymbol{p}_1 - \boldsymbol{p}_2]$ of two particles with the distance vector $\boldsymbol{r} = \boldsymbol{x}_1 - \boldsymbol{x}_2$. Since the nucleons should not be shifted apart if their distance is large, the shift function $s(r)$ is introduced.
In order to illustrate the action of the correlation operator it can be applied to a two-body state $|\psi\rangle = |\Phi_{\rm cm}\rangle \otimes |\phi\rangle$. By construction the correlator does not act on the center-of-mass component of the state. For the central correlated relative part of the state the effect of the correlation operator resembles a norm-conserving coordinate transformation [11]

$$\langle \boldsymbol{r}|C_r|\phi\rangle = \frac{R_-(r)}{r}\,\sqrt{R'_-(r)}\,\langle R_-(r)\,\frac{\boldsymbol{r}}{r}|\phi\rangle. \tag{2.7}$$

The correlation function $R_-(r)$ and its inverse $R_+(r)$ are related to the shift function $s(r)$ by the integral equation

$$\int_r^{R_\pm(r)} \frac{\mathrm{d}\xi}{s(\xi)} = \pm 1. \tag{2.8}$$

For a slowly varying shift function the correlation function is approximately given by $R_\pm(r) \simeq r \pm s(r)$.

2.3 Tensor Correlations

Besides the repulsive core, the strong tensor force is a common property of realistic nucleon-nucleon interactions. It induces a correlation between the spins $\boldsymbol{\sigma}_1$ and $\boldsymbol{\sigma}_2$ of two nucleons and their relative spatial orientation. Figure 2.2 illustrates the dependence of the interaction energy $V_T = -\left[\frac{3}{r^2}\,(\boldsymbol{\sigma}_1\cdot\boldsymbol{r})(\boldsymbol{\sigma}_2\cdot\boldsymbol{r}) - \boldsymbol{\sigma}_1\cdot\boldsymbol{\sigma}_2\right]$ of two nucleons for parallel and anti-parallel spin orientations. For spins aligned perpendicular to their connecting axis $\boldsymbol{r}$ (on the left) an anti-parallel orientation is favored. In contrast, spins aligned parallel to $\boldsymbol{r}$ prefer a parallel orientation (on the right) [12, 22, 23].

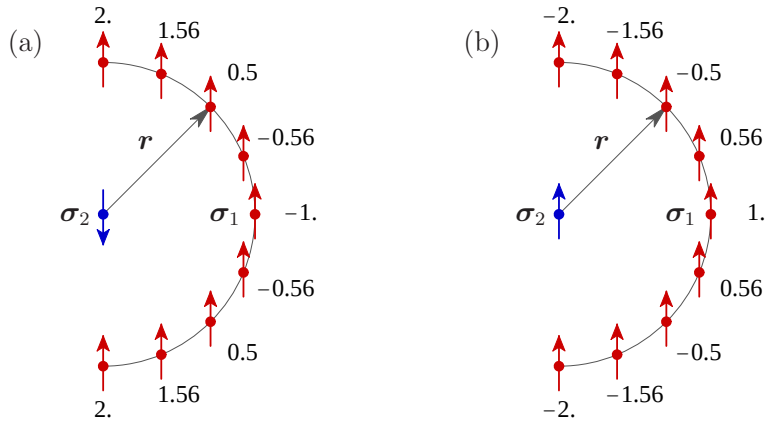

Figure 2.2: Illustration of the tensor interaction energy for fixed parallel orientation of two spins on the left and anti-parallel orientation on the right, (from [23]).

For the description of the tensor correlations the nucleons have to be shifted perpendicular to their radial direction. This can be achieved by using the orbital momentum operator

$$\boldsymbol{q}_\Omega = \boldsymbol{q} - q_r \frac{\boldsymbol{r}}{r} = \frac{1}{2\,r^2}\,(\boldsymbol{L}\times\boldsymbol{r} - \boldsymbol{r}\times\boldsymbol{L}) \tag{2.9}$$

with the relative orbital angular momentum $\boldsymbol{L} = \boldsymbol{r}\times\boldsymbol{q}$. The generator for the tensor correlation operator, which describes the connection of the spins and their relative spatial orientation, can then be constructed as

$$\begin{aligned} g_\Omega &= \vartheta(r)\, S_{12}(\boldsymbol{r}, \boldsymbol{q}_\Omega)\, \Pi_{1T} && (2.10)\\ &= \vartheta(r)\, \frac{3}{2}\, ((\boldsymbol{\sigma}_1\cdot\boldsymbol{q}_\Omega)\,(\boldsymbol{\sigma}_2\cdot\boldsymbol{r}) + (\boldsymbol{\sigma}_1\cdot\boldsymbol{r})\,(\boldsymbol{\sigma}_2\cdot\boldsymbol{q}_\Omega))\, \Pi_{1T}. && (2.11)\end{aligned}$$

Here the general definition

$$S_{12}(\boldsymbol{a},\boldsymbol{b}) = \frac{3}{2}\,[(\boldsymbol{\sigma}_1\cdot\boldsymbol{a})\,(\boldsymbol{\sigma}_2\cdot\boldsymbol{b}) + (\boldsymbol{\sigma}_1\cdot\boldsymbol{b})\,(\boldsymbol{\sigma}_2\cdot\boldsymbol{a})] - \frac{1}{2}\,(\boldsymbol{\sigma}_1\cdot\boldsymbol{\sigma}_2)\,(\boldsymbol{a}\cdot\boldsymbol{b} + \boldsymbol{b}\cdot\boldsymbol{a}) \tag{2.12}$$

is used. The tensor correlation function $\vartheta(r)$ describes the strength and the radial dependence of the transverse shift of the nucleons, analogous to the radial shift function $s(r)$ for the central correlations.

Applying the tensor correlation operator to a relative LS-coupled two-body state $|\phi(LS)JMTM_T\rangle$, where the projection quantum numbers M and M_T will be omitted for brevity, leads to [11]

$$C_\Omega|\phi(JS)JT\rangle = |\phi(JS)JT\rangle \tag{2.13}$$

for states with $J = L$ and to

$$C_\Omega|\phi(J \pm 1, 1)JT\rangle = \cos\theta_J(r)|\phi(J \pm 1, 1)JT\rangle \mp \sin\theta_J(r)|\phi(J \mp 1, 1)JT\rangle \tag{2.14}$$

for states with $L = J \pm 1$. Where the short hand notation $\theta_J(r) = 3\sqrt{J(J+1)}\vartheta(r)$ was introduced.
In Figure 2.3 the action of the central and tensor correlators is depicted. Panel (a) shows the uncorrelated deuteron wavefunction with orbital angular momentum $L = 0$. It describes the long-range behavior in a reasonable manner, but the correlation hole and the D-wave admixture are missing. The application of the central correlator with the correlation function $s(r)$, shown in (d), leads to a correlated wavefunction (b). The correlation hole has been generated by shifting the amplitude from the region with small particle distances towards distances where the potential is attractive. The application of the tensor correlator with the correlation function $\vartheta(r)$, displayed in panel (e) generates a D-wave admixture and leads to a realistic deuteron wavefunction, shown in (c). Since the tensor correlation function is long-ranged, a long-ranged D-wave admixture results [23].

2.4 Cluster Expansion

The exponential in the definition of the correlation operators (2.4) implies, that a correlated operator $\tilde{O} = C^\dagger\, O\, C$ contains irreducible contributions of all particle numbers up to A. The cluster expansion of the correlated operator

$$\tilde{O} = \tilde{O}^{[1]} + \tilde{O}^{[2]} + \ldots + \tilde{O}^{[n]} + \ldots \tilde{O}^{[A]} \tag{2.15}$$

describes the decomposition of the operator into a specific part $\tilde{O}^{[n]}$ for each particle number n. This shows, that even a correlated two-body operator contains a three-body contribution and also contributions with higher particle numbers.
Since the calculation of the third order is quite complex, a restriction to the second order would be preferable, i.e. the two-body approximation

$$\tilde{O} = \tilde{O}^{[1]} + \tilde{O}^{[2]}. \tag{2.16}$$

This is valid if the density of the system is small and the range of the correlation functions is restricted to short distances. If the correlation length is larger than the mean particle distance, the probability to find more than two nucleons in the correlation volume increases, contributions of higher orders of the cluster expansion are not negligible.

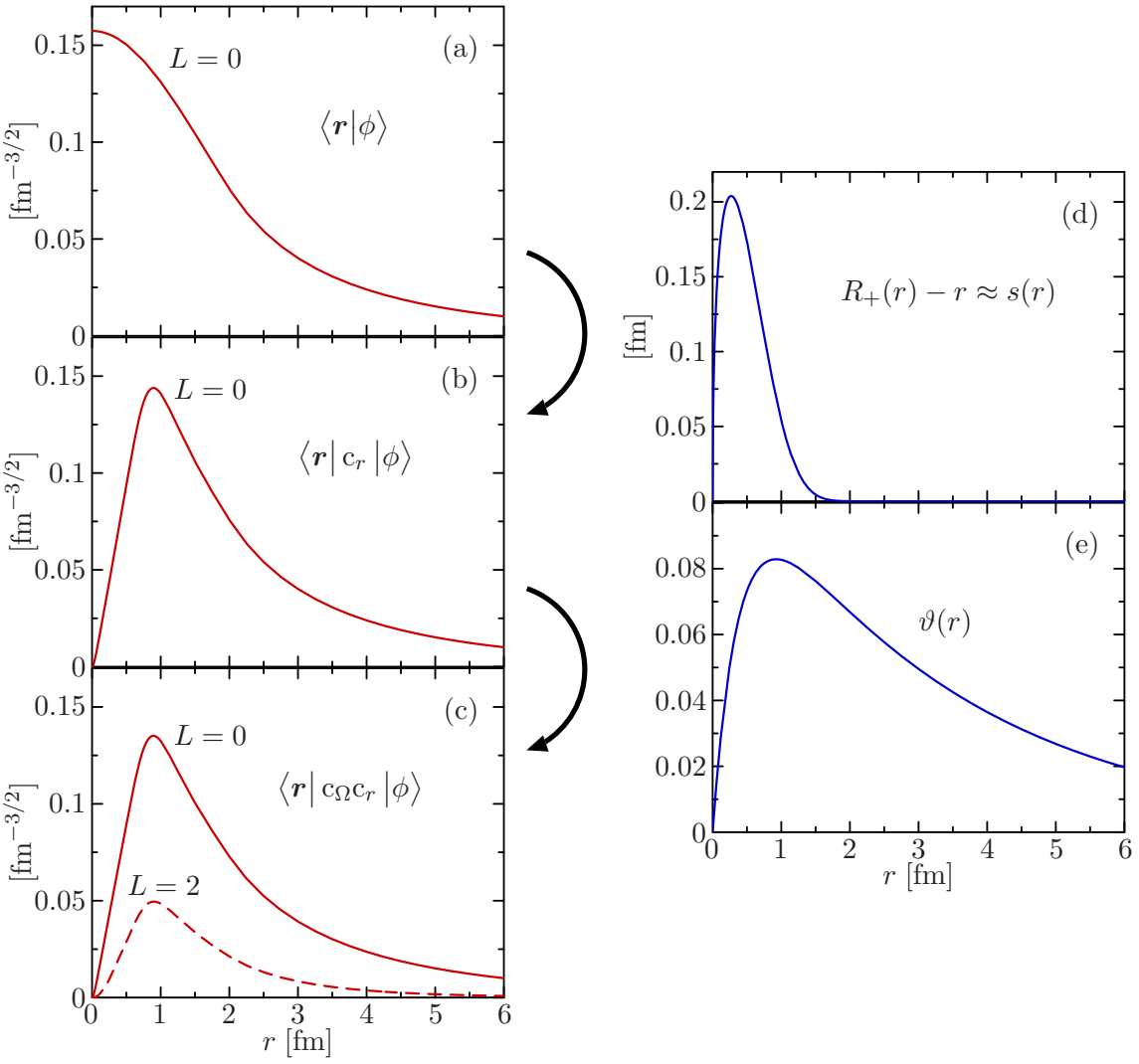

Figure 2.3: Construction of the deuteron wavefunction for the Argonne V18 potential. In panel (a) the uncorrelated wavefunction is shown. Applying the central correlator with its correlation function $s(r)$ shown in (d) leads to the central correlated wavefunction (b). Application of the tensor correlator with the correlation function $\vartheta(r)$ shown in (e) produces a D-wave admixture and leads to a realistic deuteron wavefunction (c), (from [23]).

2.5 Correlated Interactions

For the construction of a correlated Hamiltonian in two-body approximation, the uncorrelated two-body Hamiltonian

$$H = T_{\rm int} + V \equiv \frac{\boldsymbol{q}^2}{2\,\mu} + V, \tag{2.17}$$

with the intrinsic kinetic energy $T_{\rm int} = T - T_{\rm cm}$ and the two-body potential V, is chosen as a starting point. V is represented by the realistic interaction Argonne V18 for illustration. Its operator structure (see Section 1.2) is given by

$$\begin{aligned} V_{\rm Argonne} &= \sum_{S,T} \left[V^c_{ST}(r) + V^{l2}_{ST}(r)\,\boldsymbol{L}^2 \right] \Pi_{ST} \\ &+ \sum_{T} \left[V^t_T(r)\,S_{12}(\boldsymbol{r},\boldsymbol{r}) + V^{ls}_T(r)\,(\boldsymbol{L}\cdot\boldsymbol{S}) + V^{ls2}_T(r)\,(\boldsymbol{L}\cdot\boldsymbol{S})^2 \right] \Pi_{1T}, \end{aligned} \tag{2.18}$$

where charge-dependent terms have been omitted.
With the projection operator Π_S, which projects onto the spin space, the quadratic spin-orbit term can be rewritten as [23]

$$(\boldsymbol{L}\cdot\boldsymbol{S})^2 = \frac{2}{3}\,\boldsymbol{L}^2\,\Pi_1 - \frac{1}{2}\,(\boldsymbol{L}\cdot\boldsymbol{S}) + \frac{1}{6}\,S_{12}(\boldsymbol{L},\boldsymbol{L}), \tag{2.19}$$

where

$$S_{12}(\boldsymbol{L},\boldsymbol{L}) = \frac{3}{2}\,[(\boldsymbol{\sigma}_1\cdot\boldsymbol{L})\,(\boldsymbol{\sigma}_2\cdot\boldsymbol{L}) + (\boldsymbol{\sigma}_2\cdot\boldsymbol{L})\,(\boldsymbol{\sigma}_1\cdot\boldsymbol{L})] - (\boldsymbol{\sigma}_1\cdot\boldsymbol{\sigma}_2)\,\boldsymbol{L}^2. \tag{2.20}$$

The operators r, q_r^2, $\boldsymbol{L}^2$, $(\boldsymbol{L}\cdot\boldsymbol{S})$, $S_{12}(\boldsymbol{r},\,\boldsymbol{r})$ and $S_{12}(\boldsymbol{L},\,\boldsymbol{L})$ have to be correlated to determine the correlated interaction. It results

$$C_r^\dagger\, r\, C_r = R_+(r), \tag{2.21}$$

$$C_r^\dagger\, q_r^2\, C_r = \frac{1}{2}\left\{ \frac{1}{R'_+(r)^2}\,q_r^2 + q_r^2\,\frac{1}{R'_+(r)^2} \right\} + \frac{7\,R''_+(r)^2}{4\,R'_+(r)^4} - \frac{R'''_+(r)}{2\,R'_+(r)^3} \tag{2.22}$$

for the centrally correlated operators r and q_r^2. The transformation of q_r^2 generates a local potential in addition to the state-dependent part. Since all other operators act only on the angular part of the wavefunction, they are invariant under central correlations.
To find the tensor correlated operators, the Baker-Campbell-Hausdorff expansion [11, 23]

$$\begin{aligned} C_\Omega^\dagger\, O\, C_\Omega &= \exp(\mathrm{i}\,g_\Omega)\,O\exp(-\mathrm{i}\,g_\Omega) \\ &= O + \mathrm{i}\,[g_\Omega,\,O] + \frac{\mathrm{i}^2}{2}\,[g_\Omega,\,[g_\Omega,\,O]] + \ldots \end{aligned} \tag{2.23}$$

can be used.
With the tensor correlator, the correlated operators r and q_r^2 have the structure

$$C_\Omega^\dagger \, r \, C_\Omega = r, \tag{2.24}$$

$$C_\Omega^\dagger \, q_r^2 \, C_\Omega = q_r^2 - \left[\vartheta'(r)\, q_r + q_r\, \vartheta(r)\right] \, S_{12}(\boldsymbol{r}, \boldsymbol{q}_\Omega) + \left[\vartheta'(r)\, S_{12}(\boldsymbol{r}, \boldsymbol{q}_\Omega\right]^2. \tag{2.25}$$

The other operators require the full Baker-Campbell-Hausdorff expansion. At first order the commutators [11, 23]

$$\left[g_\Omega, \boldsymbol{L}^2\right] = \mathrm{i}\vartheta(r)\,(2\,\bar{s}(\boldsymbol{q}_\Omega, \boldsymbol{q}_\Omega)), \tag{2.26}$$

$$[g_\Omega, \boldsymbol{L}\cdot\boldsymbol{S}] = \mathrm{i}\vartheta(r)\,(-\bar{s}(\boldsymbol{q}_\Omega, \boldsymbol{q}_\Omega)), \tag{2.27}$$

$$[g_\Omega, S_{12}(\boldsymbol{r}, \boldsymbol{r})] = \mathrm{i}\vartheta(r)\,(-24\,\Pi_1 - 18\,(\boldsymbol{L}\cdot\boldsymbol{S}) + 3\,S_{12}(\boldsymbol{r}, \boldsymbol{r})), \tag{2.28}$$

$$[g_\Omega, S_{12}(\boldsymbol{L}, \boldsymbol{L})] = \mathrm{i}\vartheta(r)\,(7\,\bar{s}(\boldsymbol{q}_\Omega, \boldsymbol{q}_\Omega)), \tag{2.29}$$

have to be evaluated. In first order the operator

$$\bar{s}_{12}(\boldsymbol{q}_\Omega, \boldsymbol{q}_\Omega) = 2\,r^2\, S_{12}(\boldsymbol{q}_\Omega, \boldsymbol{q}_\Omega) + S_{12}(\boldsymbol{L}, \boldsymbol{L}) - \frac{1}{2}\, S_{12}(\boldsymbol{r}, \boldsymbol{r}) \tag{2.30}$$

is generated for the first time. In second order the commutator $[g_\Omega, \bar{s}(\boldsymbol{q}_\Omega, \boldsymbol{q}_\Omega)]$ has to be evaluated which generates a new operator. The generation of a new operator is repeated for each new order in the expansion. For the operator representation the Baker-Campbell-Hausdorff series has to be truncated at a certain order. To avoid this truncation several concepts can be used [11], one possibility is to calculate the two-body matrix elements directly in harmonic oscillator basis.
All these considerations lead to a correlated interaction V_{UCOM}, which is included in the correlated Hamiltonian

$$\tilde{H} = \tilde{T}^{[1]} + \tilde{T}^{[2]} + \tilde{V}^{[2]} = T + V_{\mathrm{UCOM}}. \tag{2.31}$$

The correlated and the uncorrelated one-body kinetic energies are the same, since the central correlator only contains two-body and higher terms aside from the unit operator. Together the two-body kinetic energy $\tilde{T}^{[2]}$ and the two-body potential $\tilde{V}^{[2]}$ represent the correlated interaction [11, 23]

$$\begin{aligned} V_{\mathrm{UCOM}} &= \sum_{S,T} \left[\tilde{V}_{ST}^{c}(r) + \frac{1}{2}\,\left[\tilde{V}_{ST}^{qr2}\, q_r^2 + q_r^2\, \tilde{V}_{ST}^{qr2}\right] + \tilde{V}_{ST}^{l2}(r)\, \boldsymbol{L}^2\right] \Pi_{ST} \\ &+ \sum_{T} \Big[\tilde{V}_{T}^{ls}(r)\,(\boldsymbol{L}\cdot\boldsymbol{S}) + \tilde{V}_{T}^{t}(r)\, S_{12}(\boldsymbol{r}, \boldsymbol{r}) + \tilde{V}_{T}^{tll}(r)\, S_{12}(\boldsymbol{L}, \boldsymbol{L}) \\ &+ \tilde{V}_{T}^{tqq}(r)\, \bar{s}_{12}(\boldsymbol{q}_\Omega, \boldsymbol{q}_\Omega) + \ldots\Big] \, \Pi_{1T}. \end{aligned} \tag{2.32}$$

The ellipsis denote that not all in the Baker-Campbell-Hausdorff expansion generated terms are listed here.

2.6 Correlated Two-Body Matrix Elements

In the following, two-body matrix elements of the correlated Hamiltonian will be derived. Therefore, LS-coupled states $|n(LS)JMTM_T\rangle$ are considered with relative orbital angular momentum L, spin S, total angular momentum J and isospin T with the respective quantum numbers M and M_T. The resulting matrix elements have the following structure:

$$\langle n(LS)JMTM_T|\, C_r^\dagger C_\Omega^\dagger\, H\, C_\Omega C_r\, |n'(L'S)JMTM_T\rangle. \tag{2.33}$$

Inserting harmonic oscillator states leads to:

$$\begin{aligned}\sum_{L''\,n''}\sum_{L'''\,n'''} &\langle n(LS)JT|\, C_r^\dagger C_\Omega^\dagger\, |n''(L''S)JT\rangle \\ &\times \langle n''(L''S)JT|\, H\, |n'''(L'''S)JT\rangle \\ &\times \langle n'''(L'''S)JT|\, C_\Omega C_r\, |n'(L'S)JT\rangle,\end{aligned} \tag{2.34}$$

where the projection quantum numbers M and M_T are omitted. This result can be separated into three parts, one resembling the harmonic oscillator matrix elements of the Hamiltonian and into two parts for the matrix elements for the correlation operators that are the adjoint of each other.
In the following just the first part of equation (2.34) will be considered. For computing the single matrix elements of the central and the tensor correlation operator, the insertion of the unit operator

$$\mathbb{1} = \sum_{LSJT}\int \mathrm{d}r r^2 |r(LS)JT\rangle\langle r(LS)JT| \tag{2.35}$$

leads to

$$\begin{aligned}&\langle n(LS)JT|\, C_r^\dagger C_\Omega^\dagger\, |n'(L'S)JT\rangle \\ &\qquad = \sum_{L''}\int \mathrm{d}r'' r''^2 \langle n(LS)JT|r''(L''S)JT\rangle\langle r''(L''S)JT|\, C_r^\dagger C_\Omega^\dagger\, |n'(L'S)JT\rangle.\end{aligned} \tag{2.36}$$

With equations (2.7) and (2.14) the matrix elements

$$\langle n(JS)JT|\, C_r^\dagger C_\Omega^\dagger \,|n'(JS)JT\rangle$$
$$= \int \mathrm{d}r'' r''^2 \frac{R_-(r'')}{r''} \sqrt{R'_-(r'')} \langle n(JS)JT|r''(JS)JT\rangle \langle R_-(r'')(JS)JT|n'(JS)JT\rangle \tag{2.37}$$
$$= \int \mathrm{d}r'' r''^2 \frac{R_-(r'')}{r''} \sqrt{R'_-(r'')} \phi^\dagger_{n,\,J}(r'') \phi_{n',\,J}(R_-(r'')) \tag{2.38}$$

are obtained for $L = L' = J$. Here $\phi_{n,\,L}(r)$ are the wavefunctions in the oscillator basis. For $L = L' = J \pm 1$ the following diagonal matrix elements result:

$$\langle n(J \pm 1,\, S)JT|\, C_r^\dagger C_\Omega^\dagger \,|n'(J \pm 1,\, S)JT\rangle$$
$$= \int \mathrm{d}r'' r''^2 \frac{R_-(r'')}{r''} \sqrt{R'_-(r'')} \cos\tilde{\theta}_J(r) \phi^\dagger_{n,\,J\pm1}(r'') \phi_{n',\,J\pm1}(R_-(r'')), \tag{2.39}$$

with $\tilde{\theta}_J(r) = 3\sqrt{J(J+1)}\,\vartheta(R_-(r))$. The off-diagonal matrix elements with $L = J \mp 1$ and $L' = J \pm 1$ are given by

$$\langle n(J \pm 1,\, S)JT|\, C_r^\dagger C_\Omega^\dagger \,|n'(J \mp 1,\, S)JT\rangle$$
$$= \pm \int \mathrm{d}r'' r''^2 \frac{R_-(r'')}{r''} \sqrt{R'_-(r'')} \sin\tilde{\theta}_J(r) \phi^\dagger_{n,\,J\mp1}(r'') \phi_{n',\,J\pm1}(R_-(r'')). \tag{2.40}$$

Analogous calculations can be performed for the third term of equation (2.34). With these results, the matrix elements of the transformed Hamiltonian in (2.34) can be evaluated.

2.7 Optimal Correlation Functions

In the following, the question about the optimal correlation functions $R_\pm(r)$ and $\vartheta(r)$ is treated. They should only affect short-range correlations, long-range correlations should be described by the many-body state. The correlation functions can be determined by mapping uncorrelated states onto exact two-body eigenstates of the Hamiltonian or by an energy minimization in the two-nucleon system [11]. Both methods lead to similar results. With energy minimization a correlated energy expectation value is calculated considering the lowest partial wave for each spin-isospin channel. In the case of momentum-space partial wave matrix elements with vanishing relative momenta, the expectation value of the correlated Hamiltonian is minimized by variation of the parametrizations of the central and the tensor correlation functions.
For the central correlation functions with the variational parameter sets α, β, η and α, β, γ

two possible parametrizations are used [11]:

$$R_+^{\mathrm{I}}(r) = r + \alpha \left(\frac{r}{\beta}\right)^{\eta} \exp\left\{-\exp\left\{\frac{r}{\beta}\right\}\right\} \tag{2.41}$$

$$R_+^{\mathrm{II}}(r) = r + \alpha \left(1 - \exp\left\{\frac{r}{\gamma}\right\}\right) \exp\left\{-\exp\left\{\frac{r}{\beta}\right\}\right\}. \tag{2.42}$$

For each ST-channel the parametrization that generates the lowest energy solution is chosen.

The tensor correlation function affects only channels with $S = 1$. It is parametrized by

$$\vartheta(r) = \alpha \left(1 - \exp\left\{-\frac{r}{\gamma}\right\}\right) \exp\left\{-\exp\left(\frac{r}{\beta}\right)\right\}. \tag{2.43}$$

The range of the tensor correlation function is restricted by using

$$I_\vartheta = \int \mathrm{d}r\, r^2\, \vartheta(r) \tag{2.44}$$

since only the short-range correlations should be dealt with. This is because in coordinate space the repulsive core of the central correlations ranges up to 0.5 fm, while the tensor correlations range much further. By restricting the tensor correlations a separation of scales is introduced, where the short-range correlations are described by the correlation operators, while the long-range correlations have to be described by the Hilbert space, as demanded above. A long-range tensor correlator would also depend on the considered nucleus, an extraction of state-independent correlations is only possible without long-range correlation functions [11].

Chapter 3

The Similarity Renormalization Group

3.1 The Flow Equation

In Chapter 2, the UCOM was presented as a tool to handle the short-range correlations induced by realistic nucleon-nucleon potentials. In momentum-space, the UCOM transformation causes a pre-diagonalization of the initial interaction, leading to an improvement of the convergence behavior of the correlated interaction [11]. Another method to handle these short-range properties by a pre-diagonalization of the interaction leading to a phase-shift equivalent potential is the Similarity Renormalization Group (SRG) [7, 8, 9, 10]. It will be discussed in the following.
As in the UCOM, the basic idea of the SRG is to transform an initial many-body Hamiltonian H_0 via a unitary transformation

$$H_\alpha = U_\alpha \, H_0 \, U_\alpha^\dagger \tag{3.1}$$

with the α-dependent unitary operator U_α.
A renormalization group flow equation for the Hamiltonian H_α is formulated that induces a continuous flow towards diagonal form. In the following it will be shown (see also [24]), how such a transformation has to be structured in order to cause a diagonalization.
For investigating the behavior of the transformed Hamiltonian with respect to a flow parameter α, the derivative of H_α is computed

$$\frac{\mathrm{d}H_\alpha}{\mathrm{d}\alpha} = \frac{\mathrm{d}}{\mathrm{d}\alpha}\left(U_\alpha \, H_0 \, U_\alpha^\dagger\right) \tag{3.2}$$

$$= \frac{\mathrm{d}U_\alpha}{\mathrm{d}\alpha} \, H_0 \, U_\alpha^\dagger + U_\alpha \, H_0 \, \frac{\mathrm{d}U_\alpha^\dagger}{\mathrm{d}\alpha}. \tag{3.3}$$

With the relation $U_\alpha U_\alpha^\dagger = 1$ and its derivative $\frac{\mathrm{d}}{\mathrm{d}\alpha} U_\alpha U_\alpha^\dagger = 0 \rightarrow \frac{\mathrm{d}}{\mathrm{d}\alpha} U_\alpha^\dagger = -U_\alpha^\dagger \frac{\mathrm{d}U_\alpha}{\mathrm{d}\alpha} U_\alpha^\dagger$ the previous equation can be written as

$$\frac{\mathrm{d}H_\alpha}{\mathrm{d}\alpha} = \frac{\mathrm{d}U_\alpha}{\mathrm{d}\alpha} U_\alpha^\dagger H_\alpha - H_\alpha \frac{\mathrm{d}U_\alpha}{\mathrm{d}\alpha} U_\alpha^\dagger. \tag{3.4}$$

Introducing the anti-hermitian generator $\eta_\alpha = \frac{\mathrm{d}U_\alpha}{\mathrm{d}\alpha} U_\alpha^\dagger = -\eta_\alpha^\dagger$ the initial-value problem

$$\frac{\mathrm{d}H_\alpha}{\mathrm{d}\alpha} = [\eta_\alpha, H_\alpha], \qquad H_0 = H_{\alpha=0} \tag{3.5}$$

is obtained. This flow equation generates a set of α-dependent unitarily equivalent Hamiltonians H_α.
Equation (3.5) has the structure of the Heisenberg equation for an implicit time-dependent operator A_t

$$\frac{\mathrm{d}A_t}{\mathrm{d}t} = \mathrm{i}\,[H_t, A_t]. \tag{3.6}$$

The operator A_t is obtained from the corresponding time-independent operator of the Schrödinger picture by a unitary transformation $A_t = U_t\, A_S\, U_t^\dagger$ with the time evolution operator U_t. Comparing equation (3.5) with equation (3.6) it can be observed, that the generator of the SRG flow equation can be compared to the Hamiltonian in the Heisenberg equation, while the SRG-Hamiltonian is in the same position as the operator A_t.

3.2 Diagonalization of the Hamiltonian

The next step is to define the generator η_α in a suitable way to cause the diagonalization of the Hamiltonian. Introducing a many-body basis $\{|i\rangle\}$, the diagonal part of the Hamiltonian is represented by

$$\mathrm{diag}(H_\alpha) = \sum_i |i\rangle\langle i|H_\alpha|i\rangle\langle i|. \tag{3.7}$$

There are several different choices for η_α. In the following the ansatz of Wegner [25, 26] will be discussed, where η_α is defined by the commutator of the Hamiltonian and its diagonal:

$$\eta_\alpha = [\mathrm{diag}(H_\alpha), H_\alpha]. \tag{3.8}$$

With this simple generator the effect of decreasing off-diagonal matrix elements with increasing diagonal elements can be shown directly. Therefore the generator (3.8) is inserted in the flow equation (3.5), leading to

$$\begin{aligned} \frac{\mathrm{d}\,H_\alpha}{\mathrm{d}\alpha} &= [[\mathrm{diag}(H_\alpha), H_\alpha],\, H_\alpha] \\ &= \mathrm{diag}(H_\alpha)\, H_\alpha\, H_\alpha - 2\, H_\alpha\, \mathrm{diag}(H_\alpha)\, H_\alpha + H_\alpha\, H_\alpha\, \mathrm{diag}(H_\alpha). \end{aligned} \tag{3.9}$$

Decomposing the Hamiltonian into matrix elements, the generator reads

$$\eta_{ij} = H_{ij}\,(H_{ii} - H_{jj}), \tag{3.10}$$

where the H_{ii} are the diagonal matrix elements and the H_{ij} are the off-diagonal elements of the Hamiltonian. Here the index α is omitted for brevity. Using this the matrix elements of the flow equation (3.9) with the generator (3.10) can be written as:

$$\begin{aligned}\frac{\mathrm{d}}{\mathrm{d}\alpha}H_{ij} &= \sum_k [H_{ii}\,(H_{ik} + H_{kk})(H_{kj} + H_{jj}) \\ &+ (H_{ii} + H_{ik})(H_{kj} + H_{kk})\,H_{jj} \\ &- 2\,(H_{ii} + H_{ik})\,H_{kk}\,(H_{kj} + H_{jj})]\end{aligned} \tag{3.11}$$

with $i \neq j$ for the off-diagonal matrix elements. Expanding the right ride of this equation

$$\begin{aligned}\frac{\mathrm{d}}{\mathrm{d}\alpha}H_{ij} &= \sum_k [H_{ii}\,H_{ik}\,H_{kj} + H_{ik}\,H_{kj}\,H_{jj} - H_{ik}\,H_{kk}\,H_{kj} \\ &+ H_{ii}\,H_{ik}\,H_{jj} + H_{ii}\,H_{kj}\,H_{jj} - H_{ik}\,H_{kk}\,H_{kj} \\ &- H_{ii}\,H_{kk}\,H_{kj} - H_{ik}\,H_{kk}\,H_{jj}]\end{aligned} \tag{3.12}$$

and rearranging the terms

$$\begin{aligned}\frac{\mathrm{d}}{\mathrm{d}\alpha}H_{ij} &= \sum_k [(H_{ii} + H_{jj} - 2\,H_{kk})\,H_{ik}\,H_{kj} + H_{ii}\,H_{ik}\,H_{jj} \\ &- H_{ii}\,H_{kk}\,H_{kj} + H_{ii}\,H_{kj}\,H_{jj} - H_{ik}\,H_{kk}\,H_{jj}]\end{aligned} \tag{3.13}$$

leads to an equation for the off-diagonal part:

$$\begin{aligned}\frac{\mathrm{d}H_{ij}}{\mathrm{d}\alpha} &= (H_{ii}\,H_{jj} - H_{ii}\,H_{ii} + H_{ii}\,H_{jj} - H_{jj}\,H_{jj})\,H_{ij} \\ &+ \sum_k (H_{ii} + H_{jj} - 2\,H_{kk})\;H_{ik}\,H_{kj} \qquad (3.14) \\ &= -(H_{ii} - H_{jj})^2\,H_{ij} + \sum_k (H_{ii} + H_{jj} - 2\,H_{kk})\;H_{ik}\,H_{kj}. \qquad (3.15)\end{aligned}$$

Another equation describing the behavior of the diagonal matrix elements

$$\begin{aligned}\frac{\mathrm{d}H_{ii}}{\mathrm{d}\alpha} &= \sum_k (2\,H_{ii} - 2\,H_{kk})\;H_{ik}\,H_{ki} \qquad (3.16) \\ &= 2\sum_k (H_{ii} - H_{kk})\;|H_{ik}|^2. \qquad (3.17)\end{aligned}$$

can be obtained following similar steps for $i = j$.
In order to illustrate the action of the flow equation, the equation for the diagonal matrix elements is chosen. Considering the derivative of the sum over the squares of the diagonal matrix elements H_{ii} and rearranging the terms leads to

$$\frac{\mathrm{d}}{\mathrm{d}\alpha}\sum_i H_{ii}^2 \;=\; \sum_i \frac{\mathrm{d}}{\mathrm{d}\alpha}H_{ii}^2 = \sum_i 2H_{ii}\frac{\mathrm{d}}{\mathrm{d}\alpha}H_{ii}. \tag{3.18}$$

Inserting equation (3.17) gives:

$$\begin{aligned}\frac{\mathrm{d}}{\mathrm{d}\alpha}\sum_i H_{ii}^2 &= 2\sum_{i,\,k} 2\,H_{ii}\,(H_{ii}-H_{kk})\;|H_{ik}|^2 &(3.19)\\ &= 2\sum_{i,\,k}(2\,H_{ii}\,H_{ii}-2\,H_{ii}\,H_{kk})\;|H_{ik}|^2 &(3.20)\\ &= 2\sum_{i,\,k}(H_{ii}-H_{kk})^2\;|H_{ik}|^2 \geq 0. &(3.21)\end{aligned}$$

H is hermitian, therefore its diagonal elements are real numbers whose squares are positive. The square of the absolute value of the off-diagonal elements and therefore the product of both parts is also positive. A summation of positive elements leads to an increasing result. Thus the derivative of the square of the matrix elements has to increase.
With this result it can be shown, that the off-diagonal matrix elements have to decrease. To this end the trace of the matrix is considered, which is invariant under a unitary transformation. This implies, that the derivative of the trace of this matrix has to vanish:

$$\frac{\mathrm{d}}{\mathrm{d}\alpha}\mathrm{Tr}\left(H^2\right) = \frac{\mathrm{d}}{\mathrm{d}\alpha}\sum_{i,j}\left(H_{ii}^2+|H_{ij}|^2\right) = 0. \tag{3.22}$$

Since the sum of the squares of the diagonal matrix elements has to increase as shown in equation (3.18), the off-diagonal matrix elements must decrease monotonically to satisfy equation (3.22). This shows, that the flow equation (3.5) with the generator (3.8) causes the desired diagonalization of the Hamiltonian.
For checking the former calculations, an arbitrary matrix is chosen and evolved with flow equation (3.5). The generator is chosen to be the commutator of the diagonal matrix elements and the matrix itself. In Figure 3.1(a) the original matrix is shown ($\alpha = 0$). Figures 3.1(b) to 3.1(i) show the evolution of the matrix for increasing flow parameter α. As expected, the increase of the flow parameter α causes the off-diagonal matrix elements to decrease. For large i and j the diagonal elements increase and for small i and j they decrease. This results from the fact, that during a diagonalization the eigenvalues of the matrix are written on the diagonal of the matrix. In a renormalization group flow, the eigenvalues are sorted by size during the diagonalization.

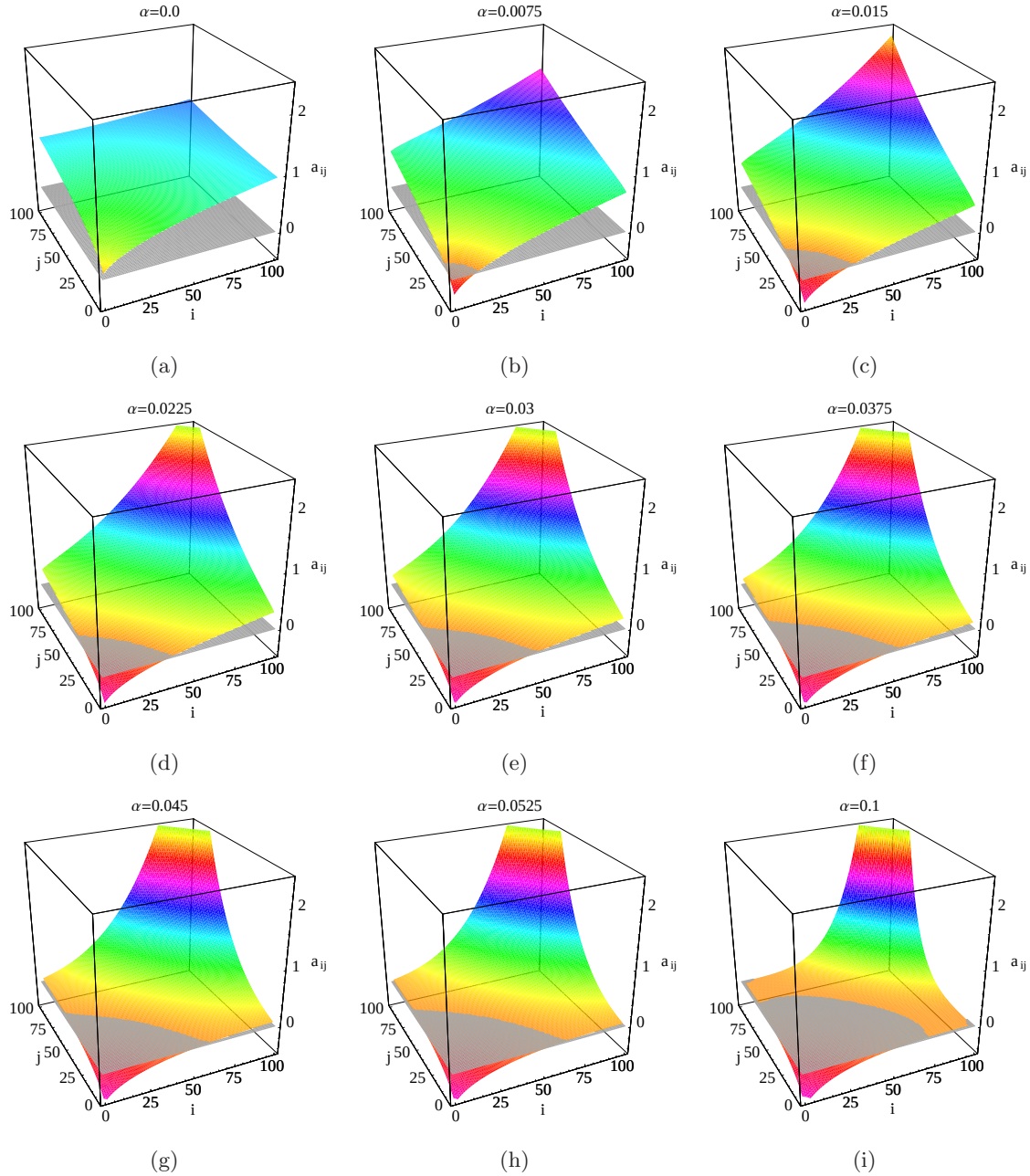

Figure 3.1: Behavior of an arbitrary matrix for increasing flow parameter α. The gray plane indicates vanishing matrix elements, i and j are the matrix indices.

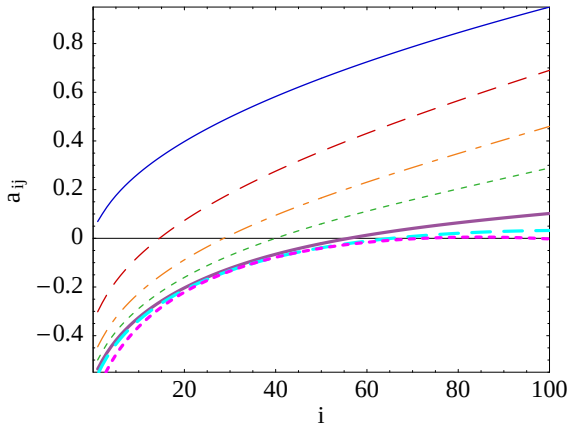

Figure 3.2: Off-diagonal matrix elements ($j = 0$) of an arbitrary matrix (——) for $\alpha = 0.0075$ (– – –), $\alpha = 0.015$ (–·–·–), $\alpha = 0.0225$ (·····), $\alpha = 0.0375$ (——), $\alpha = 0.0525$ (– – –), and $\alpha = 0.1$ (·····).

Figure 3.2 shows the off-diagonal part ($j = 0$) of the matrix used in Figure 3.1 for various values of the flow parameter α. For increasing parameters α, the matrix elements for large i decrease and converge to zero. For small i, the matrix elements become smaller for increasing flow parameter, as also seen before. This shows, that with this choice of the generator the expected diagonalization occurs even for arbitrary initial matrices.

3.3 SRG Matrix Elements in Momentum Space

Wegners choice of the generator used the commutator with the diagonal matrix elements of the Hamiltonian and the Hamiltonian itself, leading to an evolved potential V_α that contains complicated many-body interactions. Even if a two-body potential is chosen as the starting point, three-body interactions, four-body interactions and up to arbitrary many-body interactions occur during the evaluation. As a result of this, no general closed equations for the matrix elements of the interaction can be obtained. Wegner showed in [26] by solving the flow equation for each particle number separately, that the one-particle interactions are independent of the flow parameter α and the two-particle equations do not depend on higher particle numbers. Therefore, it is reasonable to work in two-body space. The solution of the flow equation is a complicated task. For simplification a matrix element representation of the problem will be discussed.
In contrast to Section 3.2 the generator η_α is chosen differently in this section. Szpigel and Perry [27] suggested a new choice for the generator, which was applied successfully by

Bogner et al. [10]. The generator reads

$$\eta_\alpha = [T_{\rm int}, H_\alpha] \tag{3.23}$$

with the relative kinetic energy $T_{\rm int} = \frac{\boldsymbol{q}^2}{2\,\mu}$, where μ is the reduced nucleon mass. This equation aims to diagonalize the Hamiltonian in a basis of eigenstates of q_r^2 and $\boldsymbol{L}^2/r^2$ respectively.
The resulting flow equation in operator representation with this new generator reads:

$$\frac{\mathrm{d}H_\alpha}{\mathrm{d}\alpha} = \left[\left[T_{\rm int}, H_\alpha\right], H_\alpha\right]. \tag{3.24}$$

Inserting a decomposition of the transformed Hamiltonian $H_\alpha = T_{\rm int} + V_\alpha$ into the kinetic energy and the α-dependent interaction V_α and evaluating the commutator leads to

$$\begin{aligned} \frac{\mathrm{d}H_\alpha}{\mathrm{d}\alpha} &= T_{\rm int}\,V_\alpha\,V_\alpha - V_\alpha\,T_{\rm int}\,T_{\rm int} + 2\,T_{\rm int}\,V_\alpha\,T_{\rm int} \\ &- 2\,V_\alpha\,T_{\rm int}\,V_\alpha - T_{\rm int}\,T_{\rm int}\,V_\alpha + V_\alpha\,V_\alpha\,T_{\rm int}. \end{aligned} \tag{3.25}$$

Evaluating this equation with the definition for $T_{\rm int}$ gives

$$\begin{aligned} \frac{\mathrm{d}}{\mathrm{d}\alpha}H_\alpha = \frac{\mathrm{d}}{\mathrm{d}\alpha}V_\alpha = &- \frac{1}{(2\,\mu)^2}\left(V_\alpha\,\boldsymbol{q}^{\,2}\,\boldsymbol{q}^{\,2} + \boldsymbol{q}^{\,2}\,\boldsymbol{q}^{\,2}\,V_\alpha - 2\boldsymbol{q}^{\,2}\,V_\alpha\,\boldsymbol{q}^{\,2}\right) \\ &+ \frac{1}{2\,\mu}\left(\boldsymbol{q}^{\,2}\,V_\alpha\,V_\alpha - 2\,V_\alpha\,\boldsymbol{q}^{\,2}\,V_\alpha + V_\alpha\,V_\alpha\,\boldsymbol{q}^{\,2}\right). \end{aligned} \tag{3.26}$$

Flow equation (3.24) generates besides the two-body interactions also higher order many-body interactions, since all many-body components of the Hamiltonian were included in this evolution. As mentioned before, good approximative results can be obtained with a two-body approximation.
With this choice of η_α (equation 3.23) it is suitable to work in momentum space. To construct a flow equation for momentum space matrix elements of the Hamiltonian, a partial-wave representation of the momentum eigenstates $|q\,(LS)JM_JTM_T\rangle$, with coupled orbital angular momentum and spin, is used. With the relation

$$\mathbb{1} = \sum_{(LS)JM_JTM_T} \int \mathrm{d}q\,q^2 |q\,(LS)JM_JTM_T\rangle\langle q\,(LS)JM_JTM_T| \tag{3.27}$$

the transformation into momentum space is accomplished. In the following the magnetic quantum numbers M_J and M_T for total angular momentum and isospin, respectively, are omitted for brevity. Inserting this identity in each term of equation (3.26) and simplifying the resulting equation, the following equation results for the uncoupled channels with

$L = L' = J$:

$$\begin{aligned}\frac{\mathrm{d}}{\mathrm{d}\alpha}V_\alpha^{(LS)JT}(q,q') &= -\frac{1}{(2\,\mu)^2}\left(q^2-q'^2\right)^2 V_\alpha^{(LS)JT}(q,q') \\ &+ \frac{1}{2\,\mu}\int \mathrm{d}q''q''^2\left(q^2+q'^2-2\,q''^2\right) V_\alpha^{(LS)JT}(q,q'')\,V_\alpha^{(LS)JT}(q'',q').\end{aligned} \tag{3.28}$$

For clarity the abbreviations

$$V_\alpha^{(LS)JT}(q,q') = \langle q\,(LS)JT|\,V_\alpha\,|q'\,(LS)JT\rangle \tag{3.29}$$

and

$$V_\alpha^{(LS)JT,\,(L'S)JT}(q,q') = \langle q\,(LS)JT|\,V_\alpha\,|q'\,(L'S)JT\rangle \tag{3.30}$$

were introduced.
For channels with $S = 1$ and $L = J \mp 1$ the insertion of (3.27) produces interaction matrix elements between states with $L = J \mp 1$ and $L' = J \pm 1$. In this case the momentum space flow equation is given by

$$\begin{aligned}\frac{\mathrm{d}}{\mathrm{d}\alpha}V_\alpha^{(LS)JT}(q,q') &= -\frac{1}{(2\,\mu)^2}\left(q^2-q'^2\right)^2 V^{(LS)JT}(q,q') \\ &+ \int \mathrm{d}q''\,q''^2\frac{1}{2\,\mu}\left(q^2+q'^2-2\,q''^2\right)\Big(V^{(LS)JT}(q,q'')\,V^{(LS)JT}(q'',q') \\ &+ V^{(LS)JT,\,(L'S)JT}(q,q'')\,V^{(L'S)JT,\,(LS)JT}(q'',q')\Big).\end{aligned} \tag{3.31}$$

For given L, the matrix elements for $L' = L \pm 2$ appear in the equation as well. The coupled channel flow equation can then be written as

$$\begin{aligned}\frac{\mathrm{d}}{\mathrm{d}\alpha}\mathcal{V}_\alpha(q,q') &= -\frac{1}{(2\,\mu)^2}\left(q^2-q'^2\right)^2 \mathcal{V}_\alpha(q,q') \\ &+ \int \mathrm{d}q''\,q''^2\frac{1}{2\,\mu}\left(q^2+q'^2-2\,q''^2\right)\mathcal{V}_\alpha(q,q'')\,\mathcal{V}_\alpha(q'',q'),\end{aligned} \tag{3.32}$$

with the matrices

$$\mathcal{V}_\alpha(q,q') = \begin{pmatrix} V^{(LS)JT,\,(LS)JT}(q,\,q') & V^{(LS)JT,\,(L'S)JT}(q,\,q') \\ V^{(L'S)JT,\,(LS)JT}(q,\,q') & V^{(L'S)JT,\,(L'S)JT}(q,\,q')\end{pmatrix}, \tag{3.33}$$

including matrix elements for different combinations of $L = J - 1$ and $L = J + 1$.
As an example the $^3\mathrm{S}_1$ partial wave of the Argonne V18 potential is shown in momentum representation for different values of the flow parameter in Figure 3.3. In the following a rescaled flow parameter $\bar{\alpha} = \frac{\alpha}{(2\,\mu)^2}$ in units of fm^4 will be used for the calculations. In Figure 3.3(a) the original matrix is shown.
In the sequence of Figures 3.3(b) to 3.3(i) the flow parameter is increased. As desired, the

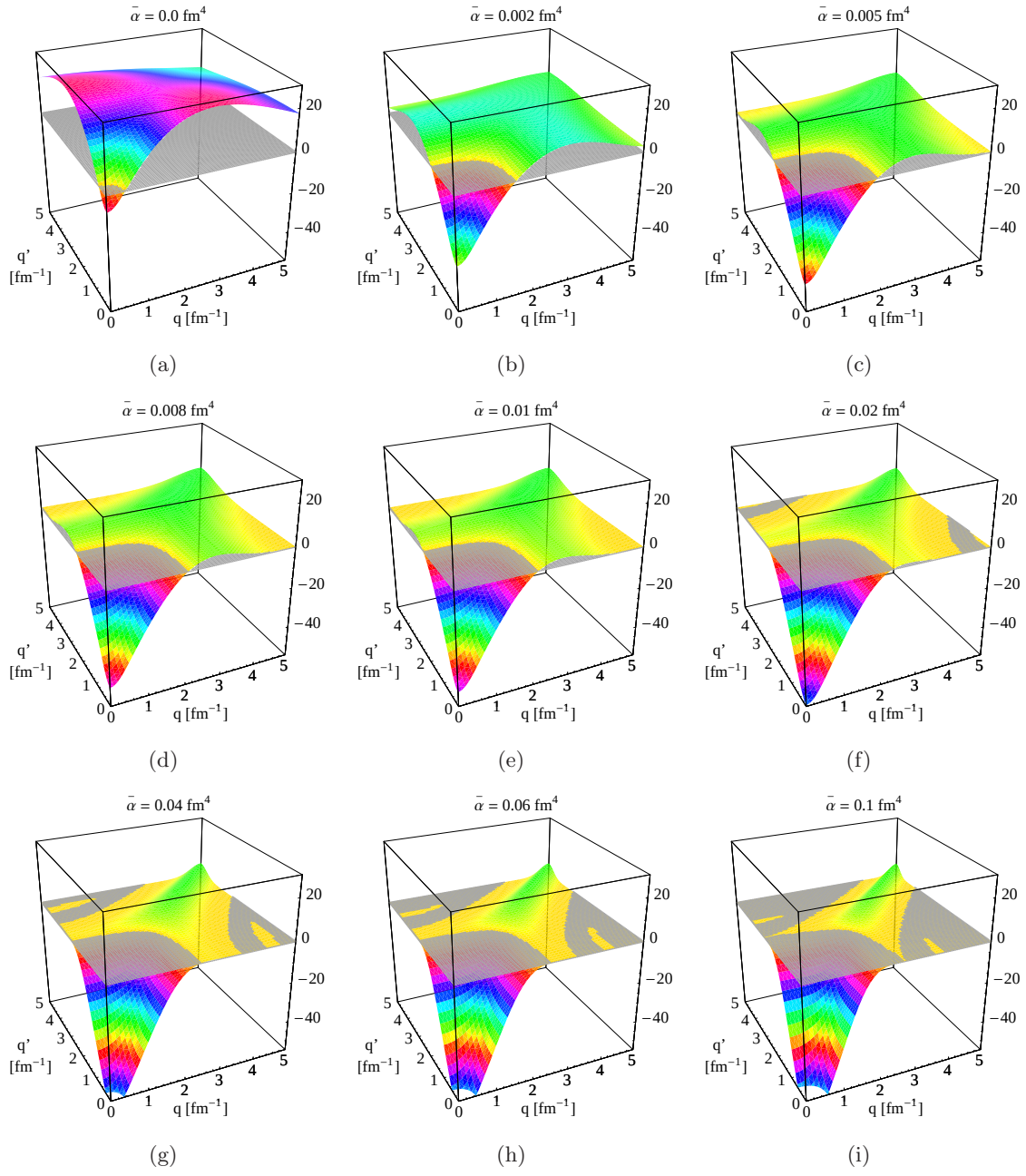

Figure 3.3: Behavior of the momentum space matrix elements $V_\alpha(q, q')$ in units of [MeV fm^3] for the $^3S_1$ partial wave of the Argonne V18 potential for different flow parameters.

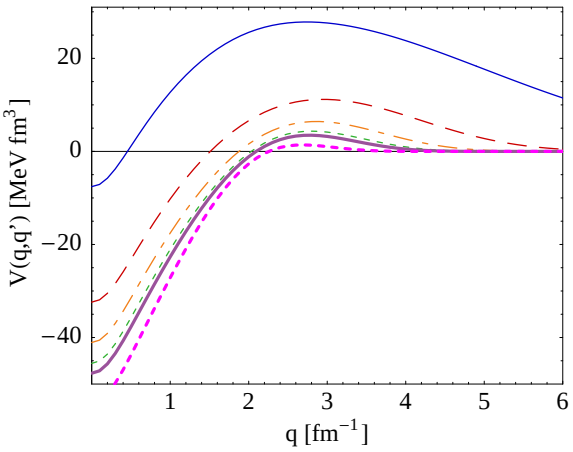

Figure 3.4: Off-diagonal matrix elements ($q' = 0\,\mathrm{fm}^{-1}$) of the $^3S_1$ partial wave of the Argonne V18 potential (——) for various flow parameters: $\bar{\alpha} = 0.01\,\mathrm{fm}^4$ (– – –), $\bar{\alpha} = 0.02\,\mathrm{fm}^4$ (–·–·–), $\bar{\alpha} = 0.04\,\mathrm{fm}^4$ (·····), $\bar{\alpha} = 0.06\,\mathrm{fm}^4$ (——), and $\bar{\alpha} = 0.1\,\mathrm{fm}^4$ (·····).

matrix *flows* towards diagonal form with increasing $\bar{\alpha}$. The diagonal matrix elements show a strong increase for large momenta and a decrease for small momenta. On the diagonal of the matrix a small band is generated. Figure 3.4 shows the off-diagonal matrix elements ($q' = 0\,\mathrm{fm}^{-1}$) of the same partial wave. For large q, the matrix elements decrease very rapidly with increasing flow parameter, for small q the values of $V(q, 0)$ decrease. This effect was also observed for the arbitrary matrix in the previous section.
In Figure 3.5(a) the deuteron wavefunction of the Argonne V18 potential is shown. For increasing flow parameter the evolution of the wavefunction leads to a shift of the D-wave component to larger radii and an elimination of the correlation hole as shown in 3.5(b). Comparing this to the UCOM transformation shown in Figure 2.3 the transformation has a similar effect.

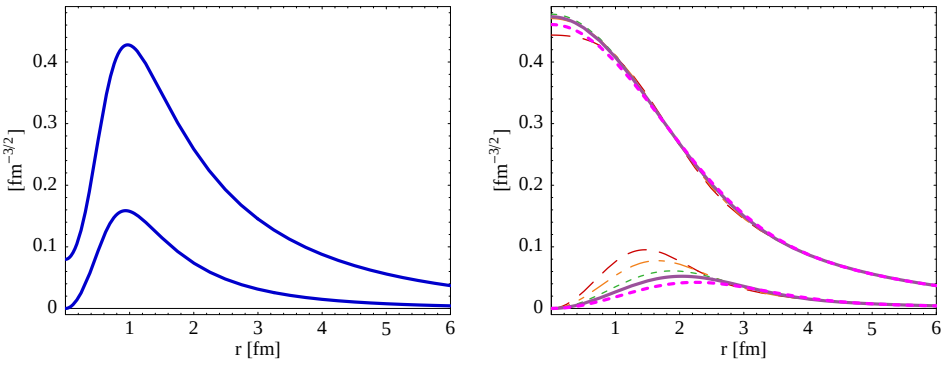

(a) Deuteron wavefunction

(b) Evolved wavefunctions

Figure 3.5: Deuteron wavefunction for the Argonne V18 potential in (a). (b) shows evolved wavefunctions for different values of the flow parameter: $\bar{\alpha} = 0.01\,\mathrm{fm}^4$ (– – –), $\bar{\alpha} = 0.02\,\mathrm{fm}^4$ (-·-·-), $\bar{\alpha} = 0.04\,\mathrm{fm}^4$ (-------), $\bar{\alpha} = 0.06\,\mathrm{fm}^4$ (———), and $\bar{\alpha} = 0.1\,\mathrm{fm}^4$ (·····).

Chapter 4

UCOM and SRG

4.1 Comparison: UCOM vs. SRG

In the previous chapters the UCOM and the SRG were discussed. Both methods use unitary transformations to decouple the low-lying states from high-lying states in order to describe the correlations that are induced by the nucleon-nucleon potentials. The unitary transformation of the UCOM describes the correlations that are induced by the short-range repulsion and the tensor interaction, leading to the transformed interaction V_{UCOM} (Chapter 2). In the SRG method the interaction is evolved via a flow equation to obtain a pre-diagonalization. Since both approaches lead to a band-diagonalized interaction, it is worthwhile to compare them to find the similarities and differences.
The realistic nucleon-nucleon potential Argonne V18 is chosen as an example. It is given by [7]

$$V_{ST} = \sum_p V_p^{ST}(r)\, O_p \tag{4.1}$$

in operator structure for a given spin-isospin (S, T)-channel. Here, only the charge-independent terms of the operator O_p are considered for simplicity, meaning

$$O_p \in \left\{1,\, \boldsymbol{L}^2,\, (\boldsymbol{L}\cdot\boldsymbol{S}),\, (\boldsymbol{L}\cdot\boldsymbol{S})^2,\, S_{12}\,(\boldsymbol{r},\boldsymbol{r})\right\}. \tag{4.2}$$

In case of the SRG, the generator (3.23) at $\bar{\alpha} = 0\,\mathrm{fm}^4$ [7]

$$\eta_0 = [T_{\mathrm{int}},\, H_0] = \frac{1}{2\,\mu}\left[q_r^2 + \frac{\boldsymbol{L}^2}{r^2},\, V_{ST}\right] \tag{4.3}$$

gives the initial flow.
This equation can be split in two commutators, one for q_r^2 and one for $\frac{\boldsymbol{L}^2}{r^2}$. For each

$(S,\,T)$-channel the commutator with the potential and q_r^2 leads to

$$\begin{aligned}\left[q_r^2,\,V_{ST}\right] &= \sum_p \left[q_r^2,\,V_p^{ST}(r)\,O_p\right] \\ &= -\mathrm{i}\sum_p (q_r\,V_p'^{ST}(r) + V_p'^{ST}(r)\,q_r)\,O_p, \end{aligned} \tag{4.4}$$

since q_r commutes with all operators of (4.2).The commutator with $\frac{\boldsymbol{L}^2}{r^2}$ results in

$$\begin{aligned}\left[\frac{\boldsymbol{L}^2}{r^2},\,V_{ST}\right] &= \left[\frac{\boldsymbol{L}^2}{r^2},\,V_t^{ST}(r)\,S_{12}(\frac{\boldsymbol{r}}{r},\,\frac{\boldsymbol{r}}{r})\right] \\ &= -4\,\mathrm{i}\frac{V_t^{ST}(r)}{r^2}\,S_{12}(\boldsymbol{r},\,\boldsymbol{q}_\Omega), \end{aligned} \tag{4.5}$$

since only the tensor component of the interaction does not commute with $\boldsymbol{L}^2$. This leads to the initial SRG-generator

$$\eta_0 = \frac{\mathrm{i}}{2}(q_r\,S(r) + S(r)\,q_r) + \mathrm{i}\Theta(r)\,S_{12}(\boldsymbol{r},\,\boldsymbol{q}_\Omega), \tag{4.6}$$

with

$$S(r) \equiv -\frac{1}{\mu}\left(\sum_p V_p'^{ST}(r)\,O_p\right) \quad \text{and} \quad \Theta(r) \equiv -\frac{2}{\mu}\frac{V_t^{ST}(r)}{r^2}. \tag{4.7}$$

The structure of the generator η_0 is similar to the sum of the UCOM generators g_r (2.5) and g_Ω (2.10). The symmetrized radial momentum q_r and the momentum-dependent tensor operator $S_{12}(\boldsymbol{r},\,\boldsymbol{q}_\Omega)$ constructed in UCOM result directly from the commutation relation that defines the generator of the flow. The SRG flow can, therefore, be connected with the central and tensor correlations in a many-body state. On the other hand this similarity confirms, that the UCOM contains all generators relevant for the description of the correlations. One difference is, that the central correlation function $s(r)$ from the UCOM is not dependent on the orbital and total angular momentum as the corresponding $S(r)$ of the SRG framework. To mimic this dependence, the correlation functions $s(r)$ in the UCOM would have to be adapted for each partial wave.

Another difference of the UCOM and the SRG approach is that in the UCOM the transformation of the Hamiltonian is accomplished in one step using a static generator. In the SRG framework, the generator η_α, starting from η_0, adapts dynamically at each step of the evolution of the Hamiltonian H_α. By assuming the SRG generator to be independent of α, the flow equation could be integrated out leading to a unitary transformation as in the UCOM scheme.

Furthermore the UCOM generators are divided to one for the central correlations and one for the tensor correlations. In the SRG method this is not distinguished. For split types, two different generators $\eta_r = \frac{1}{2\,\mu}\left[q_r^2,\,H_{\alpha_r}\right]$ and $\eta_\Omega = \frac{1}{2\,\mu}\left[\frac{\boldsymbol{L}^2}{r^2},\,H_{\alpha_\Omega}\right]$ with the flow parame-

ters α_r and α_Ω could be introduced [7].
The correlation functions of the UCOM were obtained by energy minimization so far (see Section 2.7). The tensor correlations are restricted to a range that is given by the value of I_ϑ from equation (2.44). In Figure 4.1 the $^3S_1$ partial wave in momentum space of V_{UCOM} for $I_\vartheta = 0.09\,\mathrm{fm}^3$ is compared with those of V_α for $\bar{\alpha} = 0.0208\,\mathrm{fm}^4$ and of the pure Argonne V18 potential. The value of the flow parameter is obtained by comparison of the $V(0,\,0)$ matrix elements. The matrix elements of the initial Argonne V18 potential are large in the off-diagonal region and mostly positive. In the UCOM as well as in the SRG the off-diagonal matrix elements are strongly suppressed and the part of negative matrix elements for small q and q' increases. The SRG matrix elements show a narrow band-diagonal structure for high momenta, while in the UCOM the band is much broader.

4.2 Extracting UCOM-Correlators from SRG Calculations

In the previous section the formal connection between the UCOM and the SRG method was established. The SRG approach provides the possibility to confirm that the important generators are included in the UCOM scheme, therefore a next step is to derive the UCOM correlators from the SRG. Since the UCOM correlation functions are optimized just for the lowest partial waves and are independent of the orbital angular momentum and the total angular momentum, the relevant lowest partial waves are considered for the SRG.
Considering the UCOM correlated two-body wavefunction for coupled partial waves

$$\tilde{\Phi}(r) = \begin{pmatrix} \tilde{\Phi}^{(L)}(r) \\ \tilde{\Phi}^{(L')}(r) \end{pmatrix}, \tag{4.8}$$

where $\tilde{\Phi}^{(L)}(r)$ represents the wavefunction for $L = J-1$ and $\tilde{\Phi}^{(L')}(r)$ the wavefunction for $L' = J+1$. Evaluating these with (2.7) and (2.14) leads to

$$\begin{aligned}
\tilde{\Phi}^{(L)}(r) &= \frac{R_-(r)}{r}\sqrt{R'_-(r)}\left[\cos[\theta_J(r)]\,\Phi^{(L)}\left[R_-(r)\right] + \sin[\theta_J(r)]\,\Phi^{(L')}\left[R_-(r)\right]\right] \\
\tilde{\Phi}^{(L')}(r) &= \frac{R_-(r)}{r}\sqrt{R'_-(r)}\left[-\sin[\theta_J(r)]\,\Phi^{(L)}\left[R_-(r)\right] + \cos[\theta_J(r)]\,\Phi^{(L')}\left[R_-(r)\right]\right],
\end{aligned} \tag{4.9}$$

where $\theta_J(r) = 3\sqrt{J\,(J+1)}\vartheta(R_-(r))$.
The aim is now to find the central correlation function $R_-(r)$ and the tensor correlation function $\theta_J(r)$ based on SRG calculations. For that purpose the SRG flow equation is solved for an initial interaction with a certain value of the flow parameter to obtain momentum space matrix elements $V_\alpha(q, q')$ for each partial wave. With these matrix elements the two-body problem is solved. Via a mapping of the two-body eigenstates of the SRG-evolved interaction onto the corresponding states of the initial interaction, the UCOM correlation

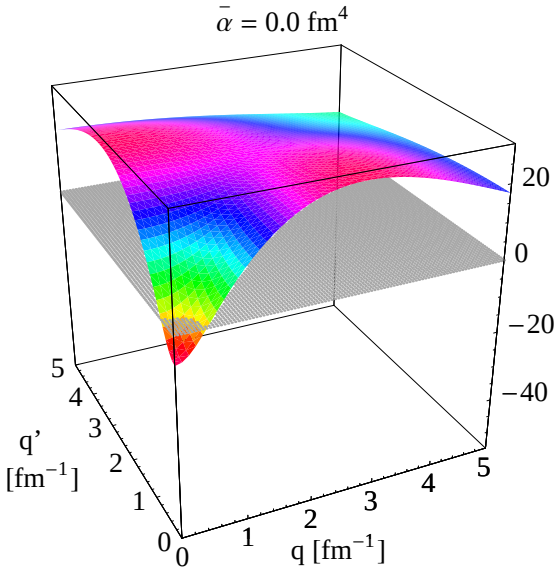

(a) Argonne V18

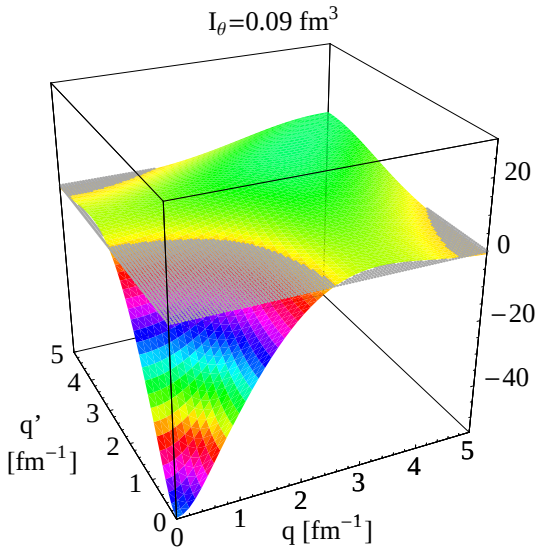

(b) UCOM

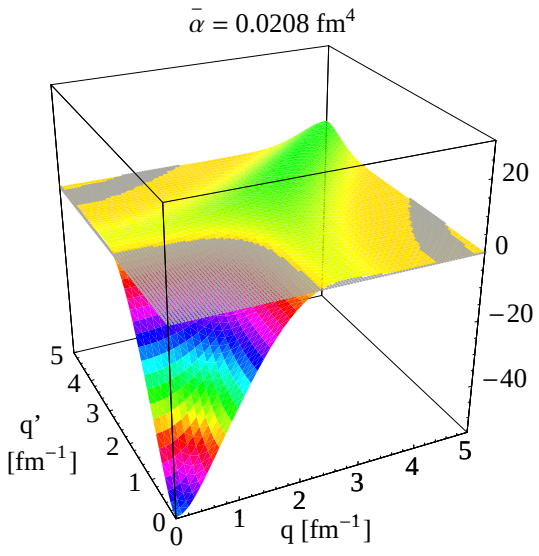

(c) SRG

Figure 4.1: Momentum space matrix elements $V_\alpha(q, q')$ in units of [MeV fm^3] of the $^3S_1$ partial wave of the Argonne V18 potential (a), the UCOM interaction with $I_\vartheta = 0.09\,\mathrm{fm}^3$ (b) and the SRG interaction with $\bar{\alpha} = 0.0208\,\mathrm{fm}^4$ (c).

functions can be obtained.
In the following the central and the tensor correlation function will be extracted separately from the partial waves. The central correlation function $R_-(r)$ acts in the same manner on the $\theta_J(r)$-dependent part of both partial waves in (4.9). Considering the sum of the squares of the absolute value of the wavefunctions leads to

$$\begin{aligned}\left|\tilde{\Phi}^{(L)}(r)\right|^2 + \left|\tilde{\Phi}^{(L')}(r)\right|^2 = \\ &\frac{R_-^2(r)}{r^2}R_-'(r)\Big\{\cos^2\theta_J(r)\,\left|\Phi^{(L)}[R_-(r)]\right|^2 + \sin^2\theta_J(r)\,\left|\Phi^{(L')}[R_-(r)]\right|^2 \\ &+ \sin^2\theta_J(r)\,\cos^2\theta_J(r)\left[\Phi^{(L)}[R_-(r)]\,\Phi^{(L')}[R_-(r)] + \Phi^{(L')}[R_-(r)]\,\Phi^{(L)}[R_-(r)]\right]\Big\} \\ &+ \frac{R_-^2(r)}{r^2}R_-'(r)\Big\{\cos^2\theta_J(r)\,\left|\Phi^{(L')}[R_-(r)]\right|^2 + \sin^2\theta_J(r)\,\left|\Phi^{(L)}[R_-(r)]\right|^2 \\ &- \sin^2\theta_J(r)\,\cos^2\theta_J(r)\left[\Phi^{(L)}[R_-(r)]\,\Phi^{(L')}[R_-(r)] + \Phi^{(L')}[R_-(r)]\,\Phi^{(L)}[R_-(r)]\right]\Big\},\end{aligned} \tag{4.10}$$

where the second and the fourth line cancel. With the relation $\sin^2[x] + \cos^2[x] = 1$ an expression independent of the tensor correlation function $\theta_J(r)$ results:

$$\left|\tilde{\Phi}^{(L)}(r)\right|^2 + \left|\tilde{\Phi}^{(L')}(r)\right|^2 = \left(\frac{R_-(r)}{r}\right)^2 R_-'(r)\left(\left|\Phi^{(L)}\,[R_-(r)]\right|^2 + \left|\Phi^{(L')}\,[R_-(r)]\right|^2\right). \tag{4.11}$$

Since the initial and the evolved wavefunctions are known, $R_-(r)$ can be evaluated by solving the following equation:

$$R_-^3(r) = 3\int_0^r \frac{\tilde{f}(r')}{f(R_-(r'))}r'^2\mathrm{d}r' \tag{4.12}$$

where the functions

$$\tilde{f}(r) = \left|\tilde{\Phi}^{(L)}(r)\right|^2 + \left|\tilde{\Phi}^{(L')}(r)\right|^2 \tag{4.13}$$

and

$$f(R_-(r)) = \left|\Phi^{(L)}(R_-(r))\right|^2 + \left|\Phi^{(L')}(R_-(r))\right|^2 \tag{4.14}$$

were introduced for simplification. The resulting integral equation can now be solved for the central correlation function.
As a next step the tensor correlation function can be determined. Since the central correlation function is obtained from equation (4.12), the tensor correlation function can be obtained by solving equations (4.9). Thus the equations for both components of the wavefunction have to be satisfied simultaneously. Solving $\tilde{\Phi}^{(L')}(r)$ for $\sin[\theta_J(r)]$ and inserting

this relation into $\tilde{\Phi}^{(L)}(r)$ leads to the relation

$$\tilde{\Phi}^{(L)}(r) = \frac{R_-(r)}{r}\sqrt{R'_-(r)}\Bigg\{\cos[\theta_J(r)\,\Phi^{(L)}\,[R_-(r)]] + \left[-\frac{\tilde{\Phi}^{(L')}(r)\,r}{R_-(r)\,\sqrt{R'_-(r)}} + \cos[\theta_J(R_-(r))]\,\Phi^{(L')}\,[R_-(r)]\right]\frac{\Phi^{(L')}\,[R_-(r)]}{\Phi^{(L)}\,[R_-(r)]}\Bigg\}, \tag{4.15}$$

which only depends on $\cos\,[\theta_J(r)]$. Due to the symmetry properties of the cosine, equation (4.15) has pairs of symmetric solutions. To find the right value for $\theta_J(r)$ the solution is reinserted in equation (4.9) to check the agreement of the UCOM transformed wavefunction with the one obtained from the SRG calculations.

4.3 Correlation Functions for Argonne V18

In this section UCOM correlators obtained from SRG calculations will be discussed for the Argonne V18 potential. In the UCOM framework the lowest partial waves of each spin-isospin channel are used to fix the correlation functions, the angular momentum dependence is omitted. Four different central correlation functions for $S = 0, 1$ and for $T = 0, 1$ and two different tensor correlation functions for $S = 1$ and $T = 0, 1$ are obtained. As a reference for comparison, the variationally optimized UCOM correlation functions (see Chapter 2) with the optimal tensor correlator for $I_\vartheta = 0.09\,\mathrm{fm}^3$ [11] will be used. They are displayed as thick solid lines in Figure 4.2 for the mentioned partial waves of the Argonne V18 potential. The central correlation functions are shown in Figures 4.2(a) - 4.2(d), the tensor correlation functions in 4.2(e) and 4.2(f) which operate only in the $S = 1$ channels. All correlation functions have a similar shape, except the tensor correlator for $(S, T) = (1, 1)$ which is set to zero for simplification, since it is an order of magnitude weaker than the tensor correlator for $(S, T) = (0, 1)$ shown in Figure 4.2(e).

In comparison to the variationally optimized correlators, the SRG-optimized ones for the Argonne V18 potential, shown in the same figure, have some differences in their behavior. Figure 4.2(a) shows the central correlator for $(S, T) = (0, 0)$ that has a similar shape, range and amplitude as its counterpart of the variationally optimized UCOM calculations. With increasing flow parameter the range of the correlation function increases. This means that the correlations of longer ranges are removed within the SRG-transformation. Another possibility to increase the range of the central correlator is via a constraint, but this will not be discussed in this thesis. The range of the variationally optimized correlators can be modified by variation of the free parameters (see Section 2.7). This would lead to a similar result.

In the $(S, T) = (0, 1)$ channel an interesting effect occurs that does not appear in any of the variationally optimized correlators: The function has a zero at about 1.2-1.3 fm,

depending on $\bar{\alpha}$. $R_+(r) - r$ describes the radial shift distance, hence the nucleons are shifted towards smaller r. This change of sign occurs in the most attractive region of the interaction, where the probability amplitude is concentrated. For distances smaller than this, probability amplitude is shifted towards larger r, for larger distances it is shifted towards smaller r. For different flow parameters, the positive part does not change, the negative component in contrast becomes stronger and its range increases. The central part of $(S,T) = (1,0)$, shown in Figure 4.2(c) has a very similar structure, also with a small negative component. A large difference between the variationally optimized UCOM results and the SRG-optimized correlations appears for $(S,T) = (1,1)$ (Figure 4.2(d)). Both correlators have about the same range, but the central correlator of $(S,T) = (1,1)$ has a large negative contribution and the positive part is much weaker than of the UCOM calculations.
The tensor correlator for $(S,T) = (1,0)$ (Figure 4.2(e)) also has a zero, but the negative contribution is much weaker than in the central correlators. The variation of the flow parameter leads to a shift of the positive and the negative peaks towards larger radii, again meaning a remote of longer ranged correlations. In Figure 4.2(f) the tensor correlator for $(S,T) = (1,1)$ is shown, which is very weak and completely negative. The major difference of the correlators of both approaches is that the variationally optimized correlators have no sign change in counterpart to the SRG-optimized correlators.

4.4 Correlation Functions for N3LO

In the previous section the SRG-optimized UCOM correlation functions were shown for the Argonne V18 potential and compared with the correlation functions obtained from variationally optimized UCOM calculations. In this section the correlation functions for the chiral N3LO potential (see Section 1.3) will be discussed.
In Figure 4.3 the correlation functions for the N3LO potential are shown. For $(S,T) = (0,0)$ the central correlation function (Figure 4.3(a)) has a similar shape as the correlation functions obtained for the Argonne V18 potential (see Section 4.3), but with a smaller amplitude. The variation of the flow parameter also leads to a shift towards larger r. In the case of $(S,T) = (0,1)$ shown in Figure 4.3(b), the correlation function starts to oscillate. This effect also occurs in the central and tensor correlator for $(S,T) = (1,0)$ (Figure 4.3(c)), where it is much stronger. The range of the correlation function is much longer than in the other cases before. Varying the flow parameter affects the whole correlator, not just the negative contribution as for the Argonne V18 potential. The central correlation function for $(S,T) = (1,1)$ is shown in Figure 4.3(d). It is completely negative and its range increases also with variation of the flow parameter.
The tensor correlation functions are both much weaker than for the Argonne V18 potential. In Figures 4.3(e) and 4.3(f) the tensor correlation functions are shown with rescaled plot

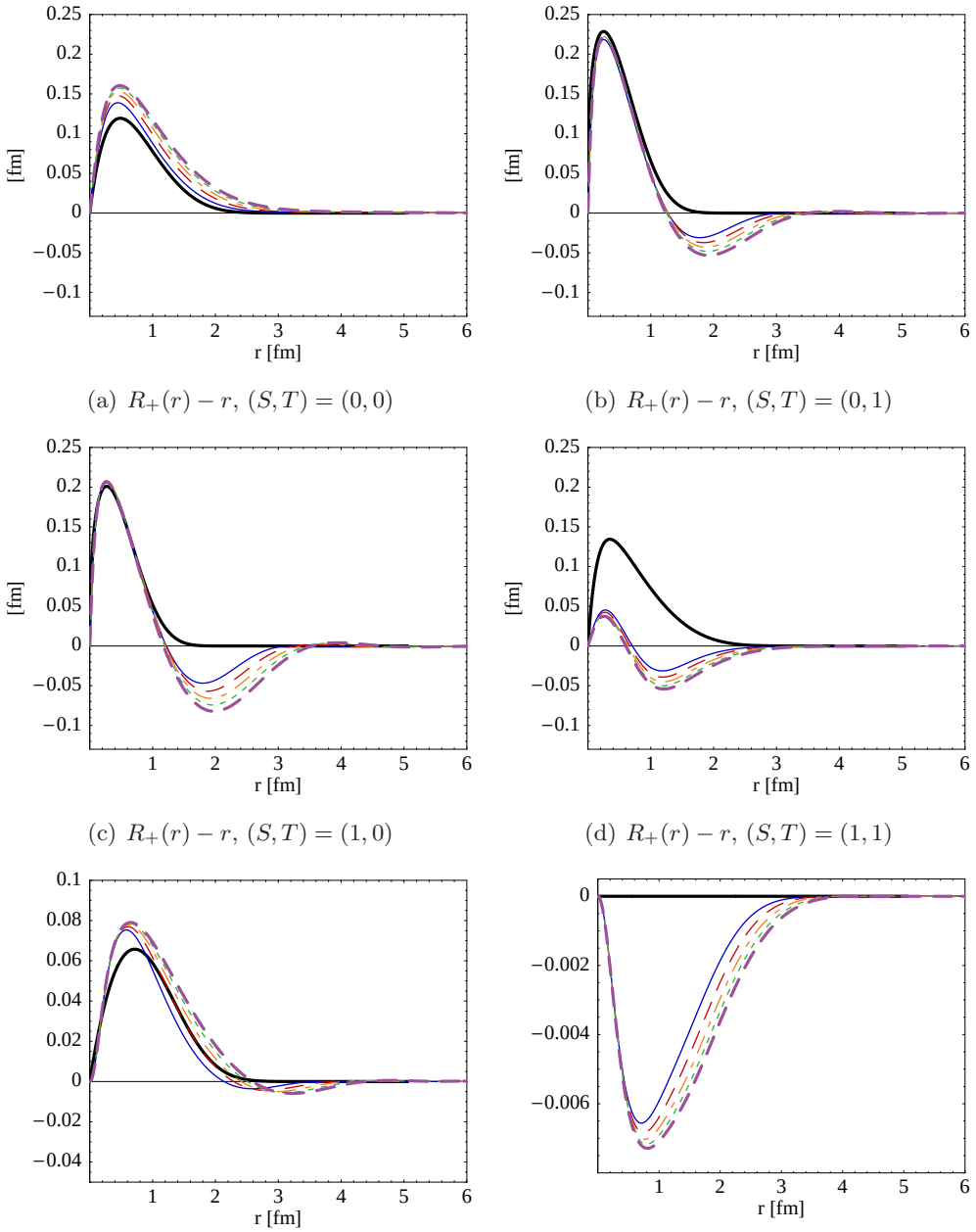

(a) $R_+(r) - r$, $(S,T) = (0,0)$

(b) $R_+(r) - r$, $(S,T) = (0,1)$

(c) $R_+(r) - r$, $(S,T) = (1,0)$

(d) $R_+(r) - r$, $(S,T) = (1,1)$

(e) $\vartheta(r)$, $(S,T) = (1,0)$

(f) $\vartheta(r)$, $(S,T) = (1,1)$

Figure 4.2: Variationally optimized and SRG-optimized UCOM correlation functions for the Argonne V18 potential. Central correlation functions for $(S,T) = (0,0)$ (a), for $(S,T) = (0,1)$ (b), for $(S,T) = (1,0)$ (c), and for $(S,T) = (1,1)$ (d). Tensor correlations functions for $(S,T) = (1,0)$ (e), and $(S,T) = (1,1)$ (f). For each partial wave $\bar{\alpha}$ is chosen to be $0.0\,\mathrm{fm}^4$ (———), $0.02\,\mathrm{fm}^4$ (– – –), $0.03\,\mathrm{fm}^4$ (-·-·-), $0.05\,\mathrm{fm}^4$ (·····), and $0.06\,\mathrm{fm}^4$ (– – –). The variationally optimized UCOM correlators are indicated by (———). Note the rescaled plot axis for the tensor correlators.

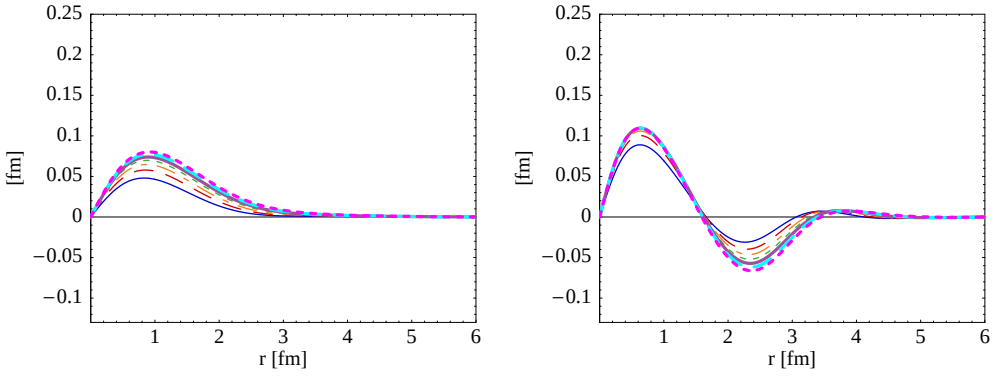

(a) $R_+(r) - r$, $(S,T) = (0,0)$

(b) $R_+(r) - r$, $(S,T) = (0,1)$

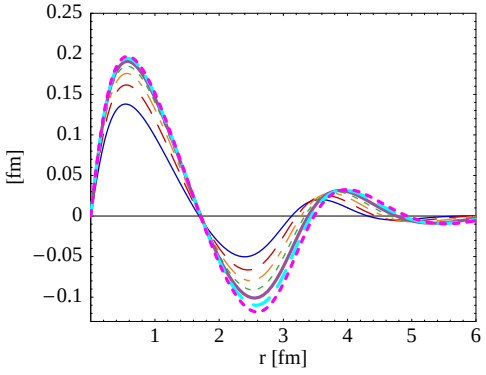

(c) $R_+(r) - r$, $(S,T) = (1,0)$

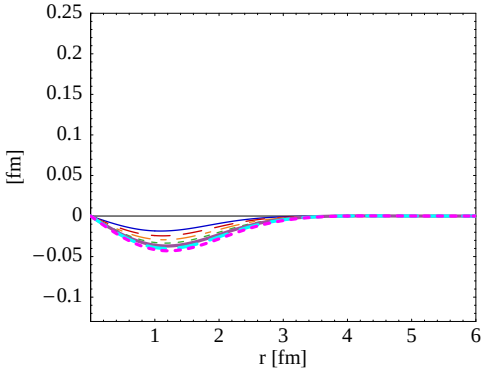

(d) $R_+(r) - r$, $(S,T) = (1,1)$

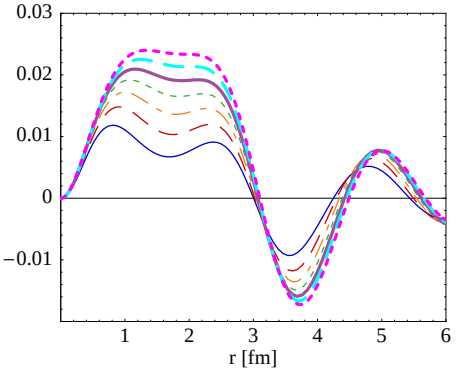

(e) $\vartheta(r)$, $(S,T) = (1,0)$

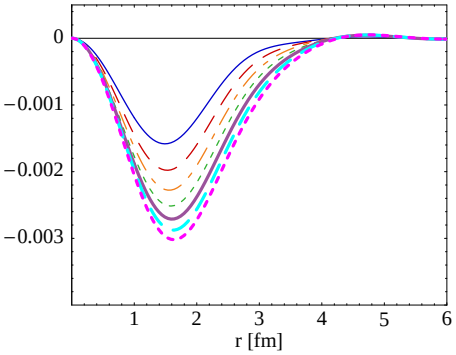

(f) $\vartheta(r)$, $(S,T) = (1,1)$

Figure 4.3: UCOM correlation functions based on SRG calculations for the N3LO potential. Central correlation functions for $(S,T) = (0,0)$ (a), for $(S,T) = (0,1)$ (b), for $(S,T) = (1,0)$ (c), and for $(S,T) = (1,1)$ (d). Tensor correlation functions for $(S,T) = (1,0)$ (e), and $(S,T) = (1,1)$ (f). For each partial wave $\bar{\alpha}$ is chosen to be $0.0\,\mathrm{fm}^4$ (——), $0.02\,\mathrm{fm}^4$ (– – –), $0.03\,\mathrm{fm}^4$ (-·-·-), $0.05\,\mathrm{fm}^4$ (·····), $0.06\,\mathrm{fm}^4$ (——), $0.07\,\mathrm{fm}^4$ (– – –), and $0.08\,\mathrm{fm}^4$ (·····). Note the rescaled plot axis for the tensor correlators.

axis. For $(S,T) = (1,0)$ the positive peak of the correlator has a dip in the middle. It seems to consist of two peaks converging for increasing flow parameter. The oscillations of this correlator are very long ranged. This is undesired since the long range correlations should not be described within the effective interactions. As for the Argonne V18 potential, the tensor correlator for $(S,T) = (1,1)$ is very weak and completely negative. The long ranged oscillations for $(S,T) = (0,1)$ and $(S,T) = (1,0)$ originate from the the wavefunctions of the N3LO potential (Section 1.3) which also show this effect.

Chapter 5

No-Core Shell Model

5.1 Basic Concepts of the No-Core Shell Model

The No-Core Shell Model (NCSM) [28, 29, 30] is a quasi-exact method for solving the nuclear many-body problem numerically with realistic nucleon-nucleon interactions. The full problem cannot be solved in the complete Hilbert space, a truncation to a finite model space is necessary. The space is constructed such that the results converge towards exact binding energies. For that purpose large Hilbert spaces have to be used. Due to limitations by computing power these calculations can only be performed for light nuclei.
The starting point for the NCSM calculations is a two-body Hamiltonian for the A-nucleon system

$$H_{\text{int}} = T_{\text{int}} + V = \frac{2}{m\,A}\sum_{i<j}^{A} \boldsymbol{q}_{ij} + \sum_{i<j=1}^{A} V_{ij}^{NN}, \tag{5.1}$$

where V_{ij}^{NN} is the nucleon-nucleon interaction.
As a basis harmonic oscillator states

$$|\psi_n\rangle = \sum_i C_{ni}|\phi_i\rangle \tag{5.2}$$

are chosen, with the evolution coefficients C_{ni} and the many-body Slater determinant

$$|\phi_n\rangle = a_{\alpha_1}^{\dagger}\cdots a_{\alpha_A}^{\dagger}|0\rangle. \tag{5.3}$$

In this basis the model space is truncated to a $N_{\max}\hbar\Omega$-space with the harmonic oscillator frequency $\hbar\Omega$ and the maximum many-body harmonic oscillator excitation energy $N_{\max}$.
Transforming the eigenvalue problem

$$H_n|\psi_n\rangle = E_n|\psi_n\rangle \tag{5.4}$$

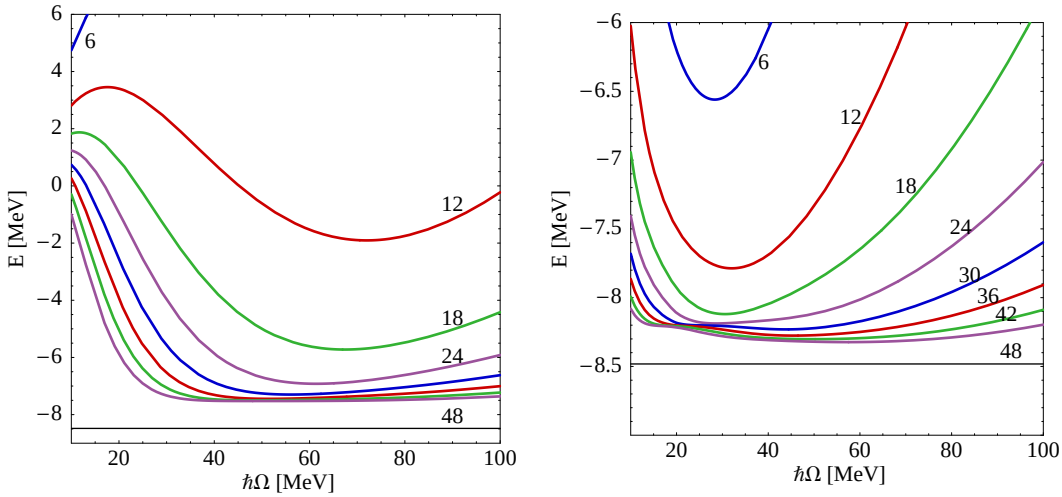

(a) Argonne V18 (b) V_{UCOM}

Figure 5.1: Convergence behavior of NCSM calculations for the ground state for different $N_{\max}\hbar\Omega$ model spaces where $N_{\max}$ ranges from 6 to 48. The results for the Argonne V18 potential on the left and V_{UCOM} for $I_\vartheta = 0.09$ fm^3 on the right are shown for ^{3}H. The horizontal line indicates the experimental binding energy.

in this basis leads to

$$H_{ij} = \langle \phi_j | H | \phi_i \rangle. \tag{5.5}$$

for the matrix elements of the Hamiltonian.

This matrix has to be diagonalized in order to obtain its eigenvalues. This is a problem since the description of the short-range repulsion requires a very large space. For that purpose effective potentials are introduced. They can be obtained by a Lee-Suzuki transformation [30, 31] or from SRG and UCOM transformations in this thesis. These methods pre-diagonalize the interaction meaning, that smaller model spaces are necessary.

5.2 NCSM Calculations for ^{3}H and ^{4}He

In this section the convergence behavior of NCSM calculations for the SRG-optimized UCOM potential, the SRG potential and the variationally optimized UCOM potential will be compared for different $N_{\max}\hbar\Omega$ model spaces for the nuclei ^{3}H and ^{4}He.

The results of the NCSM calculations for ^{3}H with the Argonne V18 potential are shown in Figure 5.1(a). The labels in the plot indicate the different values of $N_{\max}$, ranging from 6 to 48. Convergence only occurs for large values of $N_{\max} \geq 30$. In Figure 5.1(b) the behavior with the variationally optimized UCOM potential for $I_\vartheta = 0.09$ fm^3 is shown for comparison. In this case the minimum of the curve for $N_{\max} = 6$ is at about -6.5 MeV, the Argonne V18 potential in comparison is still unbound in this case. A good aspect of the

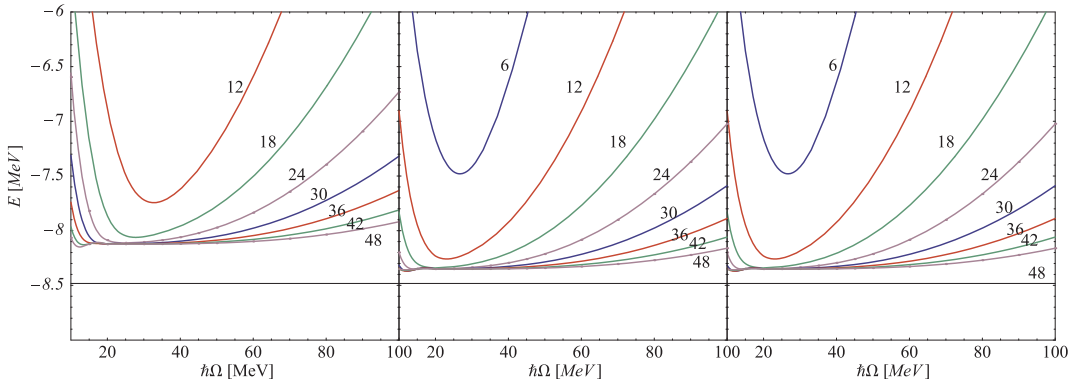

Figure 5.2: Convergence behavior of NCSM calculations for the ^{3}H ground state for different $N_{\max}\hbar\Omega$ model spaces where $N_{\max}$ ranges from 6 to 48. The results for the SRG potential for $\bar{\alpha} = 0.01$ fm^4 (left), $\bar{\alpha} = 0.03$ fm^4 (middle) and $\bar{\alpha} = 0.06$ fm^4 (right) are shown.

UCOM transformed potential is that it leads to bound states even for $0\hbar\Omega$. In this case the space consists of one Slater determinant, thus no correlations can be described. This shows, that the components of the Argonne V18 potential that induce the short-range correlations are reduced in the many-body states by the unitary transformation. One undesired property of the variationally optimized UCOM potential is that a two minima structure occurs for $N_{\max} \simeq 24$ which disappears for larger model spaces.

The NCSM calculations with the SRG potential [32] are shown in Figure 5.2 for $\bar{\alpha} = 0.01\,\text{fm}^4$, $0.03\,\text{fm}^4$ and $0.06\,\text{fm}^4$. Variation of $\bar{\alpha}$ leads to a faster convergence and a lowering of the resulting energy. The change for $\bar{\alpha} = 0.01$ fm^4 towards $\bar{\alpha} = 0.03$ fm^4, where the converged energy decreases significantly, is more significant than the difference of the results for $\bar{\alpha} = 0.03$ fm^4 and $\bar{\alpha} = 0.06$ fm^4.

For all values of $\bar{\alpha}$ there is only one minimum and the converged energy is quite constant over a wide range of frequencies $\hbar\Omega$. For the SRG-optimized UCOM potential, similar results are achieved as shown in Figure 5.3 for $\bar{\alpha} = 0.01\,\text{fm}^4$, $0.04\,\text{fm}^4$ and $0.06\,\text{fm}^4$. The converged energy lowers for increasing $\bar{\alpha}$ and good convergence is achieved for an extended range of frequencies. In all cases the experimental result cannot be described by the calculations.

In the case of ^{4}He the convergence behavior of the ground-state energy is shown for $N_{\max} = 0 \ldots 16$. The results for the Argonne V18 potential (Figure 5.4(a)) do not converge in the considered range. For small values of $N_{\max}$ the nuclei are unbound. In comparison, the results with variationally optimized UCOM correlators for $I_\vartheta = 0.09$ fm^3 are shown in Figure 5.4(b) in more detail. It shows a very good convergence to the experimental binding energy. Comparing this to the results with the SRG potential for $\bar{\alpha} = 0.01\,\text{fm}^4$, $0.03\,\text{fm}^4$, and $0.06\,\text{fm}^4$ (shown in Figure 5.5) an improved convergence can be observed. For $al\bar{p}ha =$

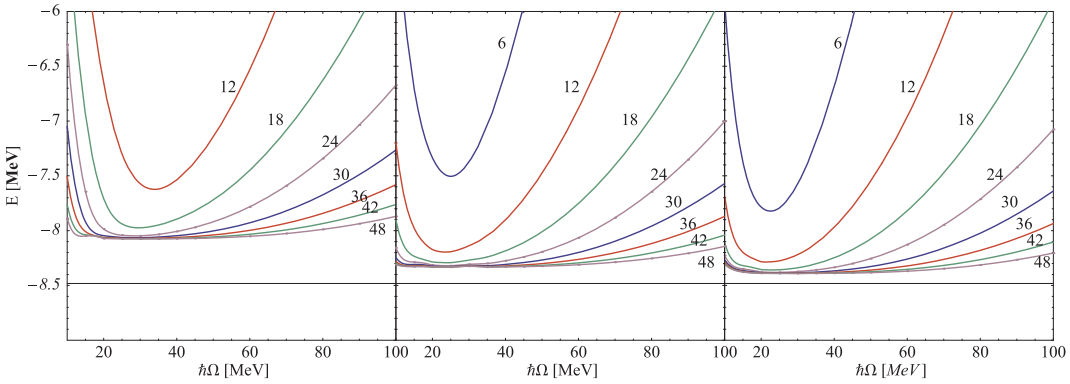

Figure 5.3: Convergence behavior of NCSM calculations for the ^{3}H ground state for different $N_{\max}\hbar\Omega$ model spaces where $N_{\max}$ ranges from 6 to 48. The results for the SRG-optimized UCOM potential for $\bar{\alpha} = 0.01$ fm^4 (left), $\bar{\alpha} = 0.04$ fm^4 (middle) and $\bar{\alpha} = 0.06$ fm^4 (right) are shown.

0.01 fm^4 the experimental value of the binding energy is not achived yet. In the case of $\bar{\alpha} = 0.03$ fm^4, the exact binding energy is obtained even faster than in the case of the variationally-optimized UCOM potential. For $al\bar{p}ha = 0.06\,\text{fm}^4$ with values of $N_{\max} \geq 6$, the calculations lead to an overbinding of the nuclei. In Figure 5.6 the SRG-optimized UCOM potential is displayed. Here the results are only slightly different from the SRG potential. Calculations for $\bar{\alpha} = 0.01$ fm^4 produce similar results as with the SRG potential. The obtained binding energies are a bit smaller in case of the SRG potential. For $\bar{\alpha} = 0.04$ fm^4 the binding energy of ^{4}He is obtained. In comparison to the variationally-optimized potential a faster convergence occurs. This may result from the negative contribution of $R_+(r) - r$, as discussed in Section 4.3. For $al\bar{p}ha = 0.06\,\text{fm}^4$ the nuclei are slightly overbound, but a good convergence is obtained also in this case.

To test if the oscillations of the correlation functions improve convergence, a function can be fit to them to cut the oscillations of $R_+(r) - r$ and $\vartheta(r)$ to obtain functions with similar shapes as in the variationally optimized UCOM framework. NCSM calculations with these new correlators show that the obtained effect is quite large. The convergence behavior of the new resulting SRG-optimized UCOM correlation functions is not that good as it was before. Therefore these correlation functions will not be used for further calculations. The oscillations in the correlation functions seem to be the reason for the improvement of the convergence, since they are the main difference to the variationally optimized ones.
For the chiral N3LO potential the oscillations in the correlators that are generated by the oscillations in the wavefunctions lead to convergence problems in further calculations. It will need investigations on this to find a way to handle this potential in an appropriate way.
In practical applications the parameters $\bar{\alpha}$ and I_ϑ are fixed to reproduce the experimental

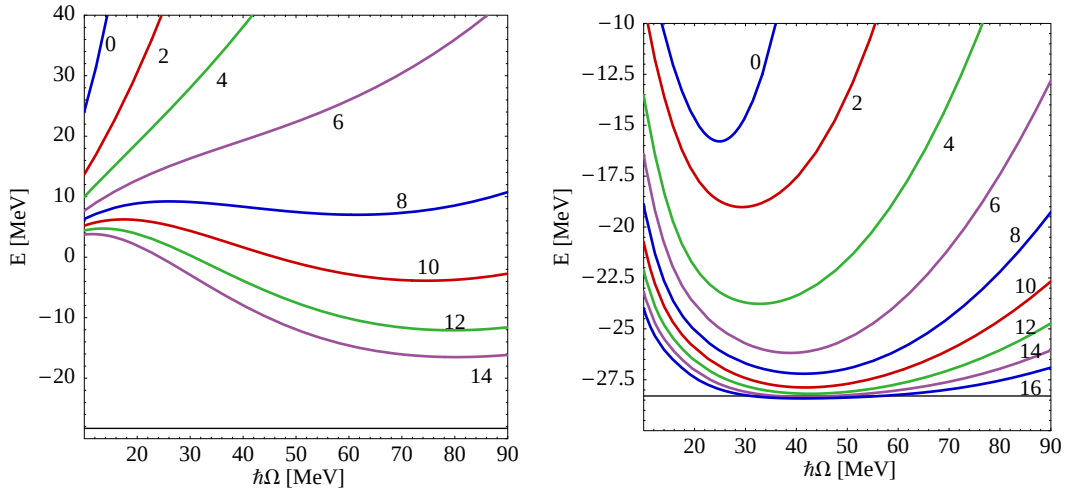

(a) Argonne V18 (b) V_{UCOM}

Figure 5.4: Convergence behavior of NCSM calculations for the ^{4}He ground state for different $N_{\max}\hbar\Omega$ model spaces where $N_{\max}$ ranges from 0 to 16. Results for the Argonne V18 potential on the left and V_{UCOM} for $I_\vartheta = 0.09$ fm^3 on the right.

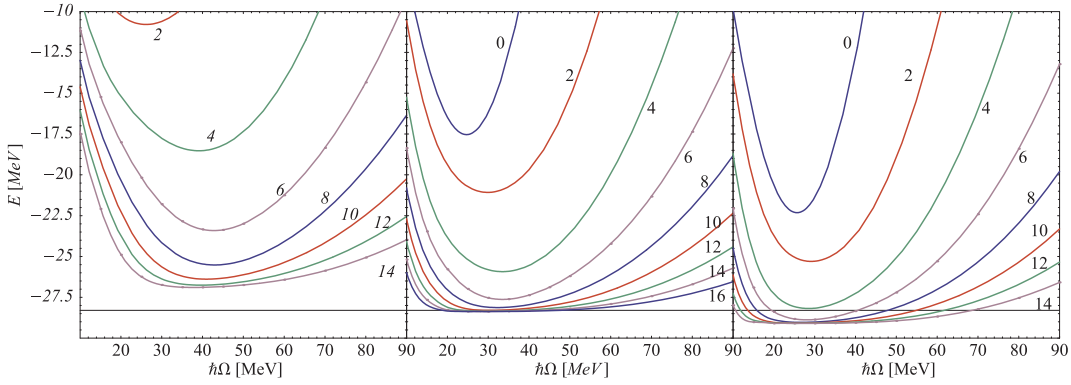

Figure 5.5: Convergence behavior of NCSM calculations for the ^{4}He ground state for different $N_{\max}\hbar\Omega$ model spaces where $N_{\max}$ ranges from 0 to 16. The results for the SRG potential for $\bar{\alpha} = 0.01$ fm^4 (left), $\bar{\alpha} = 0.03$ fm^4 (middle) and $\bar{\alpha} = 0.06$ fm^4 (right) is shown.

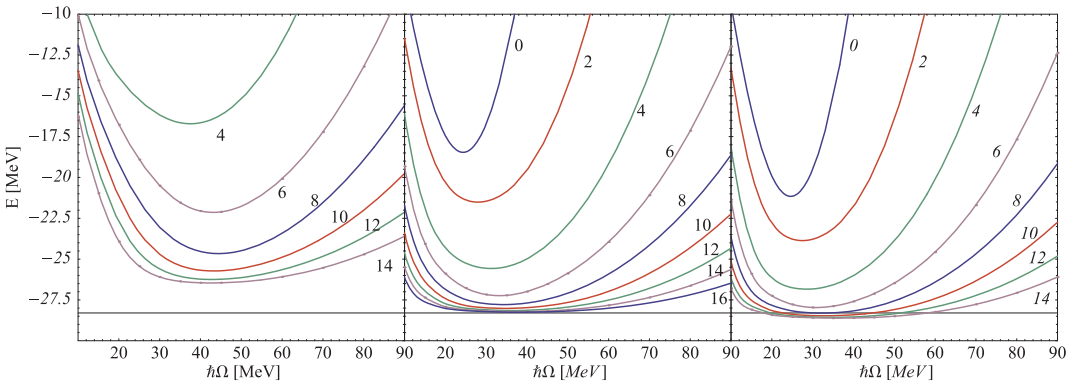

Figure 5.6: Convergence behavior of NCSM calculations for the ^{4}He ground state for different $N_{\max}\hbar\Omega$ model spaces where $N_{\max}$ ranges from 0 to 16. The results for the SRG-optimized UCOM potential for $\bar{\alpha} = 0.01$ fm^4 (left), $\bar{\alpha} = 0.04$ fm^4 (middle) and $\bar{\alpha} = 0.06$ fm^4 (right) is shown.

^{4}He binding energy. This leads to the optimal values $\bar{\alpha} = 0.03$ fm^4 for the SRG potential, $\bar{\alpha} = 0.04$ fm^4 for the SRG-optimized UCOM potential, and $I_\vartheta = 0.09$ fm^3 for the variationally optimized UCOM potential [11].

Chapter 6

Hartree-Fock

6.1 The Hartree-Fock Method

In the previous section the NCSM was introduced. Since this exact method is not applicable for heavy nuclei, a more severe approximation is required. For that purpose the Hartree-Fock method, which is based on a variational principle, will be used [33]. In the Hartree-Fock method the many-body state is described by a single Slater determinant corresponding to a $0\hbar\Omega$ space level, since no correlations can be described. At this level the UCOM and SRG transformed interactions give bound states in the NCSM calculations, therefore this should also happen in the Hartree-Fock approach. To include additional long-range correlations larger model spaces are considered in the NCSM. For heavier nuclei the many-body perturbation theory or Random-Phase Approximation could be applied to cover these correlations, but these approaches will not be discussed in this thesis. In the following the Hartree-Fock method will be discussed briefly.
The variational principle states that solving the eigenvalue problem

$$H|\Psi\rangle = E|\Psi\rangle \tag{6.1}$$

is equivalent to the variation

$$\delta E[|\Psi\rangle] = E[|\Psi\rangle + |\delta\Psi\rangle] - E[|\Psi\rangle] = 0, \tag{6.2}$$

where the energy

$$E[|\Psi\rangle] = \frac{\langle\Psi|H|\Psi\rangle}{\langle\Psi|\Psi\rangle} \tag{6.3}$$

is assumed to be a functional of the state $|\Psi\rangle$. If E is an eigenvalue of the system, the variation δE with the corresponding eigenstate $|\Psi\rangle$ is stationary. Therefore, $E[|\Psi\rangle]$ has an absolute minimum for the ground state and a saddle point for excited states [12, 13].
Ritz' variational principle is often used to construct approximative solutions of the eigen-

value problem. Therefore instead of the general states of the whole Hilbert space, trial states are introduced that cover just a subspace. If the exact eigenstate is not contained in this subspace an approximate solution is obtained.
The variational approach has the following important property: the energy expectation value $E[|\Psi_v\rangle]$ of arbitrary trial state $|\Psi_v\rangle$ is always greater than or equal to the exact ground-state energy E_0 [12, 13]:

$$E[|\Psi_v\rangle] \geq E_0. \tag{6.4}$$

This shows that the better $E[|\Psi_v\rangle]$ approximates the exact ground-state energy E_0, the greater is the overlap of the exact ground state with the trial state.
The Hartree-Fock trial state is represented by a single Slater determinant

$$|\Phi\rangle = a_1^\dagger \, a_2^\dagger \cdots a_A^\dagger |0\rangle = |\alpha_1 \cdots \alpha_A\rangle_a. \tag{6.5}$$

For determining the minimal energy expectation value $E[|\Phi\rangle]$ the single-particle states $|\alpha_i\rangle = a_i^\dagger|0\rangle$ are varied. These new states $|\alpha_i\rangle$ are expanded in a configuration space basis $\{|\chi_k\rangle\}$ with $|\chi_k\rangle = c_k^\dagger|0\rangle$:

$$|\alpha_i\rangle = \sum_k C_k^{(i)} |\chi_k\rangle \qquad \text{or} \qquad a_i^\dagger = \sum_k C_k^{(i)} c_k^\dagger. \tag{6.6}$$

The $C_k^{(i)}$ are expansion coefficients that have to be determined.
One characteristic of the Slater determinant is its invariance under unitary transformations among the occupied single-particle states [12, 13]. This means that the Slater determinant is defined by a subspace in the single-particle space and by a projection operator ρ on this subspace. Its matrix elements can be expressed in terms of the expansion coefficients $C_k^{(i)}$ and define the single-particle density matrix:

$$\rho_{kk'} = \langle\Phi|c_{k'}^\dagger c_k|\Phi\rangle = \sum_{i,i'} C_{k'}^{(i')^*} C_k^{(i)} \langle\Phi|a_{i'}^\dagger a_i|\Phi\rangle = \sum_i^A C_{k'}^{(i)^*} C_k^{(i)}. \tag{6.7}$$

The variation is carried out under the constraint of hermiticity ($\rho_{k',k}^* = \rho_{k',k}$) and idempotence ($\sum_l \rho_{kl}\rho_{lk'} = \rho_{kk'}$) of the density matrix.
Expressing the Hamiltonian in second quantization in the basis $\{|\chi_k\rangle\}$, leads to

$$H = \sum_{k_1,k_2} t_{k_1,k_2} c_{k_1}^\dagger c_{k_2} + \frac{1}{4} \sum_{k_1,k_2,k_3,k_4} V_{k_1k_2,k_3k_4} c_{k_1}^\dagger c_{k_2}^\dagger c_{k_4} c_{k_3}, \tag{6.8}$$

where $t_{k_1,k_2} = \langle\chi_{k_1}|t|\chi_{k_2}\rangle$ are the single-particle matrix elements of the kinetic energy and $v_{k_1k_2,k_3k_4} =_a \langle\chi_{k_1}\chi_{k_2}|V|\chi_{k_3}\chi_{k_4}\rangle_a$ are the two-body matrix elements of the interaction

between the nucleons. The expectation value of the Hamiltonian is

$$\begin{aligned} E[|\Phi\rangle] &= \langle\Phi|H|\Phi\rangle \\ &= \sum_{k_1,k_2} t_{k_1,k_2}\langle\Phi|c^\dagger_{k_1}c_{k_2}|\Phi\rangle + \frac{1}{4}\sum_{k_1,k_2,k_3,k_4} V_{k_1k_2,k_3k_4}\langle\Phi|c^\dagger_{k_1}c^\dagger_{k_2}c_{k_4}c_{k_3}|\Phi\rangle. \end{aligned} \tag{6.9}$$

The expectation values of the creation and annihilation operator in the basis $\{|\chi_k\rangle\}$ can be identified with the single-particle density matrix ρ_{k_2,k_1} and the two-body density matrix $\rho^{(2)}_{k_3k_4,k_1k_2} = \rho_{k_3,k_1}\rho_{k_4,k_2} - \rho_{k_3,k_2}\rho_{k_4,k_1}$. Using this the energy can be expressed as an functional of the single-particle density matrix:

$$E[\rho] = \sum_{k_1,k_2} t_{k_1,k_2}\rho_{k_2,k_1} + \frac{1}{2}\sum_{k_1,k_2,k_3,k_4} \rho_{k_3,k_1}V_{k_1k_2,k_3k_4}\rho_{k_4,k_2}. \tag{6.10}$$

Variation of this functional, where terms in quadratic order of $\delta\rho$ were discarded, gives

$$\begin{aligned} \delta E[\rho] &= \sum_{k_1,k_3} t_{k_1,k_3}\delta\rho_{k_3,k_1} + \sum_{k_1,k_2,k_3,k_4} \delta\rho_{k_3k_1}V_{k_1k_2,k_3k_4}\rho_{k_4k_2} && (6.11)\\ &= \sum_{k_1,k_3} h_{k_1,k_3}[\rho]\delta\rho_{k_3,k_1}, && (6.12) \end{aligned}$$

where $h_{k_1,k_3}[\rho] = t_{k_1,k_3} + \sum_{k_2,k_4} v_{k_1k_2,k_3k_4}\rho_{k_4,k_2}$ represents the matrix elements of a single-particle Hamiltonian with kinetic energy and a density-dependent potential.
In the Hartree-Fock basis, the single-particle density matrix is diagonal, therefore it connects only occupied states. To fulfill hermiticity and idempotence, the variation $\delta\rho$ must occur only between occupied and unoccupied states.
In the Hartree-Fock single-particle basis the variational equation results to

$$\delta E[\tilde{\rho}] = \sum_{i_1,i_3} \tilde{h}_{i_1,i_3}[\tilde{\rho}]\delta\tilde{\rho}_{i_1,i_3} = 0, \tag{6.13}$$

where $\tilde{\rho}_{i,i'}$ is the single-particle density matrix and $\tilde{h}_{i,i'}$ is the single-particle Hamiltonian in the Hartree-Fock basis. As a result the most general Hartree-Fock equation, a basis independent operator equation [12, 13]

$$[h[\rho], \rho] = 0 \tag{6.14}$$

is obtained.
The many-body problem is reduced to a single-particle eigenvalue problem in the Hartree-Fock approximation:

$$h[\rho]|\alpha_i\rangle = \epsilon_i|\alpha_i\rangle. \tag{6.15}$$

The $|\alpha_i\rangle$ are the Hartree-Fock eigenstates and the ϵ_i represent the Hartree-Fock single-particle energies. Expanding in the basis $\{|\chi_k\}$ leads to

$$\sum_{k_3} h_{k_1,k_3}[\rho] C^{(i)}_{k_3} = \epsilon_i C^{(i)}_{k_1}. \tag{6.16}$$

With the explicit form of the Hamiltonian and of the single-particle density, it gives

$$\sum_{k_3} \left(t_{k_1,k_3} + \sum_{k_2,k_4} \sum_{i'=1}^{A} V_{k_1 k_2, k_3 k_4} C^{(i')}_{k_2} C^{(i')}_{k_4} \right) C^{(i)}_{k_3} = \epsilon_i C^{(i)}_{k_1}. \tag{6.17}$$

The single-particle Hamiltonian depends on the density matrix, therefore this eigenvalue problem is non-linear for the single-particle energies ϵ_i and for the expansion coefficients $C^{(i)}_k$.
The energy of the ground state can be expressed as

$$\begin{aligned} E[|\mathrm{HF}\rangle] &= \langle \mathrm{HF}|H|\mathrm{HF}\rangle & (6.18)\\ &= \sum_{i=1}^{A} \langle \alpha_i|t|\alpha_i\rangle + \frac{1}{2} \sum_{i,i'=1}^{A} {}_a\langle \alpha_i \alpha_{i'}|V|\alpha_i \alpha_{i'}\rangle_a \\ &= \sum_{i=1}^{A} \epsilon_i - \frac{1}{2} \sum_{i,i'=1}^{A} {}_a\langle \alpha_i \alpha_{i'}|V|\alpha_i \alpha_{i'}\rangle_a. & (6.19) \end{aligned}$$

This shows, that the total energy is not given by the sum of the single-particle energies.

6.2 Hartree-Fock with Correlated Interactions

In the last section the general formulation of the Hartree-Fock method was introduced, in the following this method will be applied to correlated realistic nucleon-nucleon interactions in the UCOM framework.
The correlated Hamiltonian consists of the kinetic energy T and the correlated interaction V_{UCOM}. The center-of-mass kinetic energy T_{cm} is subtracted from the kinetic energy, which leads to the intrinsic Hamiltonian [34]

$$H_{\mathrm{int}} = T - T_{\mathrm{cm}} + V_{\mathrm{UCOM}} = T_{\mathrm{int}} + V_{\mathrm{UCOM}}. \tag{6.20}$$

The intrinsic kinetic energy can be expressed by the two-body momentum operator $\boldsymbol{q}$:

$$T_{\mathrm{int}} = T - T_{\mathrm{cm}} = \frac{2}{A\,m} \sum_{i<j}^{A} \boldsymbol{q}^2_{ij}. \tag{6.21}$$

With this, the intrinsic Hamiltonian has no single-particle kinetic energy, it is a pure two-body operator.
The harmonic oscillator states $|nljmm_t\rangle$, where n is the radial quantum number, l is the orbital angular momentum, j is the total angular momentum with projection m and m_t is the isospin projection quantum number, are used to expand the Hartree-Fock states:

$$|\nu ljmm_t\rangle = \sum_n C_n^{(\nu ljmm_t)} |nljmm_t\rangle. \tag{6.22}$$

It is assumed that due to spherical symmetry oscillator states with the same l, j, and m can contribute to the expansion of the Hartree-Fock states only. Furthermore, the following calculations will be restricted to closed shells, where the evolution coefficient is independent of m ($C_n^{(\nu ljmm_t)} = C_n^{(\nu ljm_t)}$). These expansion coefficients are the variational parameters for the minimization of the energy expectation value.
In this representation, the Hartree-Fock equation (6.16) becomes

$$\sum_{\bar{n}} h_{n\bar{n}}^{(ljm_t)} C_{\bar{n}}^{(\nu ljm_t)} = \epsilon^{(\nu ljm_t)} C_{\bar{n}}^{(\nu ljm_t)}, \tag{6.23}$$

where $\epsilon^{(\nu ljm_t)}$ are the single-particle energies of the Hartree-Fock states. The matrix elements of the single-particle Hamiltonian are given by

$$h_{n\bar{n}}^{(ljm_t)} = \sum_{l',j',m_t'} \sum_{n',\bar{n}'} H_{nn',\bar{n},\bar{n}'}^{(ljm_t,l'j'm_t')} \rho_{n',\bar{n}'}^{(l'j'm_t')}, \tag{6.24}$$

with the single-particle density matrix

$$\rho_{n',\bar{n}'}^{(l'j'm_t')} = \sum_{\nu} O^{(\nu ljm_t)} C_{\bar{n}}^{(\nu ljm_t)^*} C_n^{(\nu ljm_t)}, \tag{6.25}$$

where $O^{(\nu ljm_t)}$ is the number of occupied magnetic sublevels in the respective shell [34]. For closed shells $O^{(\nu ljm_t)}$ is equal to $2j+1$.
The m-averaged antisymmetric two-body matrix elements of the Hamiltonian can be written as [34]:

$$H_{nn',\bar{n},\bar{n}'}^{(ljm_t,l'j'm_t')} = \frac{1}{(2j+1)(2j'+1)} \sum_{m,m'} \langle nljmm_t, n'l'j'm'm_t' | H_{\text{int}} | \bar{n}ljmm_t, \bar{n}'l'j'm'm_t' \rangle. \tag{6.26}$$

The single-particle angular momenta can be coupled to a total angular momentum

$$\begin{aligned} H_{nn',\bar{n},\bar{n}'}^{(ljm_t,l'j'm_t')} = & \sum_{J,M,M_T} \frac{(2J+1)}{(2j+1)(2j'+1)} c \left(\begin{array}{cc|c} \frac{1}{2} & \frac{1}{2} & T \\ m_t & m_t' & M_T \end{array} \right)^2 \\ & \times \langle nlj, n'l'j'; JTM_T | H_{\text{int}} | \bar{n}lj, \bar{n}'l'j'; JTM_T \rangle, \end{aligned} \tag{6.27}$$

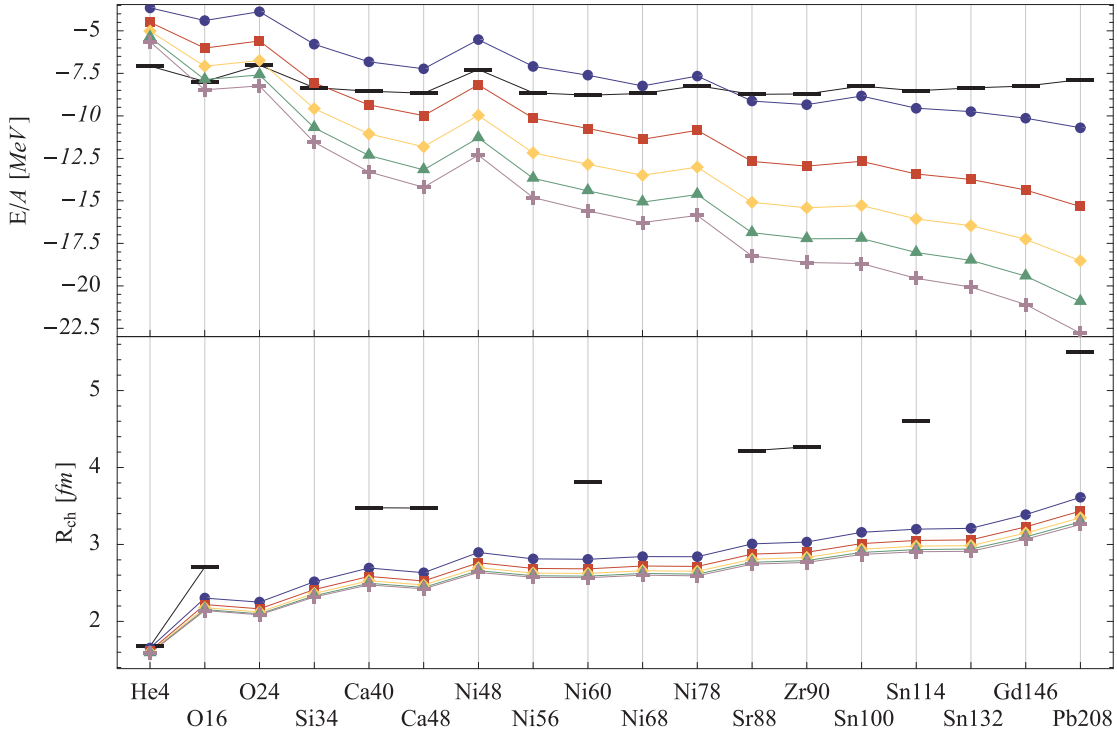

Figure 6.1: Hartree-Fock calculations with the SRG potential for $\bar{\alpha} = 0.02$ fm^4 (●), $\bar{\alpha} = 0.03$ fm^4 (■), $\bar{\alpha} = 0.04$ fm^4 (♦), $\bar{\alpha} = 0.05$ fm^4 (▲) and $\bar{\alpha} = 0.06$ fm^4 (✚). The black bars indicate experimental values.

where the Clebsch-Gordan coefficients are defined by

$$\begin{aligned} |\tfrac{1}{2}\tfrac{1}{2}, TM_T\rangle &= \sum_{m_t, m_t'} |\tfrac{1}{2}m_t, \tfrac{1}{2}m_t'\rangle\langle\tfrac{1}{2}m_t, \tfrac{1}{2}m_t'|\tfrac{1}{2}\tfrac{1}{2}, TM_T\rangle \\ &= \sum_{m_t, m_t'} c \left(\begin{array}{cc|c} \frac{1}{2} & \frac{1}{2} & T \\ m_t & m_t' & M_T \end{array} \right) |\tfrac{1}{2}m_t, \tfrac{1}{2}m_t'\rangle. \end{aligned} \tag{6.28}$$

6.3 Hartree-Fock Calculations

In the following the Hartree-Fock framework of Section 6.2 will be applied to the calculations of ground-state properties for selected closed-shell nuclei from ^{4}He to ^{208}Pb.
As basis states the eigenstates of the harmonic oscillator are chosen. The parameter $e_{\max}$ is the maximal number of eigenstates of the harmonic oscillator which are superposed to represent the singe-particle states that compose the Hartree-Fock state. The oscillator length a_{HO} and the size of the basis $e_{\max}$ are set to be $a_{\mathrm{HO}} = 1.7$ fm and $e_{\max} = 10$.
Hartree-Fock calculations with the SRG-evolved potential are shown in Figure 6.1 for $\bar{\alpha}$ ranging from 0.02 fm^4 up to 0.06 fm^4. The binding energy per nucleon, in the upper part

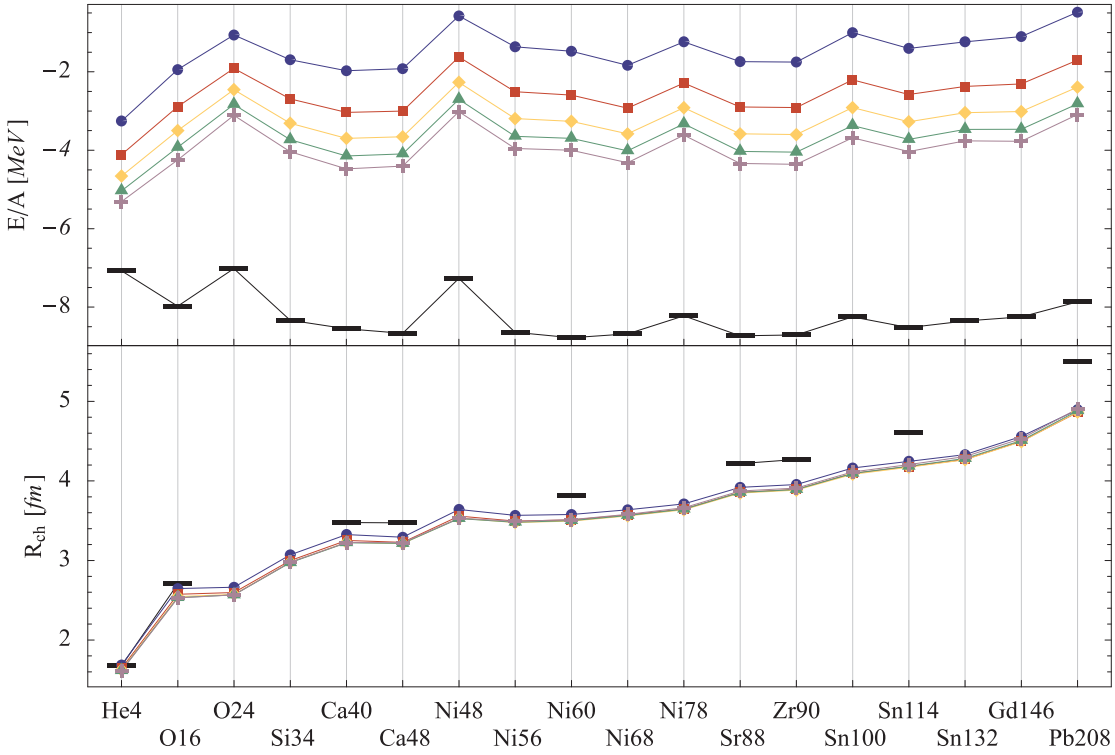

Figure 6.2: Hartree-Fock calculations with the SRG-optimized UCOM potential for $\bar{\alpha} = 0.02$ fm^4 (●), $\bar{\alpha} = 0.03$ fm^4 (■), $\bar{\alpha} = 0.04$ fm^4 (♦), $\bar{\alpha} = 0.05$ fm^4 (▲) and $\bar{\alpha} = 0.06$ (✚).

of the figure, has a similar structure as the experimental binding energy per nucleon but tilts towards larger binding energies for heavier nuclei. With increasing flow parameter the tilting increases. The charge radii are much too small for heavier nuclei and with increasing flow parameter they drift further away from the experimental values. In comparison, the Hartree-Fock results with the SRG-optimized UCOM potential show several important differences. The binding energy per nucleon and the charge radii for the examined nuclei are shown in Figure 6.2 for values of the flow parameter $\bar{\alpha}$ ranging from 0.02 fm^4 up to 0.06 fm^4. They follow the structure of the experimental results but the binding energy is too small. For increasing flow parameter the results shift towards stronger binding, but even these results do not reproduce the experimental binding energies. This constant shift compared to experimental data can be compensated with many-body perturbation theory or Random-Phase Approximation where long-range correlations are included. Experimental charge radii are reproduced much better than for the SRG potential, but they are still somewhat too small for heavy nuclei. The variation of the flow parameter does not change much on this effect.

Figure 6.3 compares the SRG potential with $\bar{\alpha} = 0.03$ fm^4, the SRG-optimized UCOM potential with $\bar{\alpha} = 0.04$ fm^4 and the variationally optimized potential with $I_\vartheta = 0.09$ fm^3.

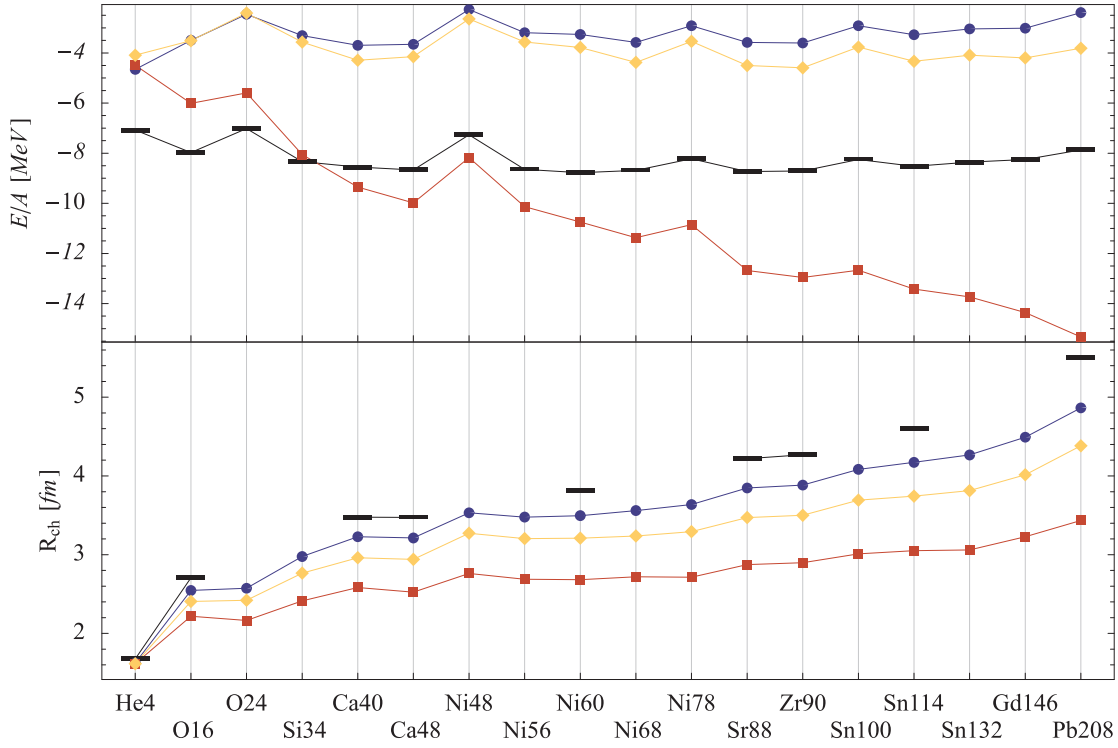

Figure 6.3: Comparison of the Hartree-Fock results for the SRG potential for $\bar{\alpha} = 0.03$ fm^4 (■), the UCOM potential with $I_\vartheta = 0.09$ fm^3 (♦) and the SRG-optimized UCOM potential with $\bar{\alpha} = 0.04$ fm^4 (●).

The results for variationally optimized and SRG-optimized UCOM are similar, while for SRG the observed tilt causes a completely different behavior. In the charge radii the SRG results are again much worse than for variationally optimized and SRG-optimized UCOM. For SRG-optimized calculations the description of heavy nuclei is even better than in the variationally optimized framework. The difference of the behavior of the two approaches can result from the treatment of all partial waves in the SRG framework, while only the lowest partial waves are considered in UCOM calculations. Another possibility is the different high-momentum behavior of the the matrix elements (see Figure 4.1). Here a narrow band is generated, thus a decoupling of all momenta in the SRG framework while the band is much broader for UCOM calculations, connecting different momentum states. Improvements for the behavior of the SRG potential could be obtained with the inclusion of a three-body interaction that is strongly repulsive [35, 32]. In the UCOM framework the tensor correlations are chosen such that three-body effects are minimized. An additional three-body component will not have a large effect. For the SRG results this interaction will cause a repulsion for heavy nuclei, a tilt towards smaller binding energies. Another point is the optimization of the parameters I_ϑ and $\bar{\alpha}$ for the ^{4}He ground state energy, which does not guarantee that they are valid for heavier nuclei as well.

Including many-body perturbation theory and Random-Phase Approximation [34, 36], the results for the UCOM potentials can be improved. A constant shift of the binding energies leads to a very close approximation of the experimental values. In contrast to that the effect of these methods on the SRG potential leads to an even stronger overbinding of the nuclei than in the Hartree-Fock scheme. This shows the necessity of including the three-nucleon force to correct for this overbinding effect.

Chapter 7

Summary and Outlook

The main goals in this work are the investigation of the SRG as a method to derive an effective potential and the connection of this approach with the results obtained within the UCOM. In the UCOM framework the short-range central and tensor correlations generated by the nucleon-nucleon interactions are treated explicitly. With this method, a correlated interaction based on the Argonne V18 potential was constructed. As another approach to handle the short-range correlations, the SRG was introduced, a method to derive an effective potential by pre-diagonalizing the initial one. The diagonalization which is induced by a continuous transformation, was analyzed for the Argonne V18 potential. The resulting interaction was investigated in NCSM calculations and the Hartree-Fock method. The convergence behavior of NCSM calculations with the SRG potential is very good, but Hartree-Fock calculations show a strong overbinding for heavier nuclei. To resolve this a three-body interaction would have to be introduced.

A comparison of UCOM and SRG indicates that both approaches are formally related. Within the SRG framework new UCOM correlation functions were constructed for the Argonne V18 potential and the chiral N3LO potential. These optimized correlation functions show differences in their structure in comparison to the variationally optimized correlation functions used previously e.g. in the form of a negative contribution that was not considered in the former parametrizations. In the case of the N3LO potential the correlation functions show very long-ranged oscillations that result from the structure of the initial potential (wavefunctions). Further investigations are necessary in order to deal with these effects in an appropriate manner.

The SRG-optimized correlation functions were used to construct a new potential V_{UCOM} from the Argonne V18 interaction which exhibits a significantly better convergence behavior in NCSM calculations than the previous variationally optimized UCOM interaction. This improvement results from the negative contribution in the correlation functions.

Hartree-Fock calculations with the new V_{UCOM} show the same trends for the binding energies as for the old V_{UCOM} potential. The charge radii are significantly closer to the

experimental values. For further improvements, many-body perturbation theory and resummation of the perturbation series in Brueckner Hartree-Fock or Random-Phase Approximation calculations can and will be used.
Furthermore the effect of a three-nucleon force onto the calculations has to be studied. This will show for the SRG if the overbinding of nuclei in Hartree-Fock calculations can be eliminated or if there is still something missing to correct for this effect.

Bibliography

[1] R. B. Wiringa, V. G. J. Stoks, and R. Schiavilla, "An accurate nucleon-nucleon potential with charge independence breaking," *Phys. Rev.*, vol. C51, pp. 38–51, 1995.

[2] R. Machleidt, "Nuclear forces from chiral effective field theory," 2007, arXiv:0704.0807 [nucl-th].

[3] R. Roth, "Die Methode der untären Korrelatoren und ihre Anwendung auf kurzreichweitig abstoßende Nukleon-Nukleon-Wechselwirkungen," diploma thesis, TH Darmstadt, 1997.

[4] T. Neff and H. Feldmeier, "Tensor correlations in the unitary correlation operator method," *Nucl. Phys.*, vol. A713, pp. 311–371, 2003.

[5] H. Feldmeier, T. Neff, R. Roth, and J. Schnack, "A unitary correlation operator method," *Nucl. Phys.*, vol. A632, pp. 61–95, 1998.

[6] T. Neff, *Short-Ranged Central and Tensor Correlations in Nuclear Many-Body Systems*. PhD thesis, TU Darmstadt, 2002.

[7] H. Hergert and R. Roth, "The unitary correlation operator method from a similarity renormalization group perspective," *Phys. Rev.*, vol. C75, p. 051001, 2007.

[8] S. K. Bogner, R. J. Furnstahl, R. J. Perry, and A. Schwenk, "Are low-energy nuclear observables sensitive to high- energy phase shifts?," *Phys. Lett.*, vol. B649, pp. 488–493, 2007.

[9] R. J. Perry and S. Szpigel, "A new renormalization group for Hamiltonian field theory," 1999, nucl-th/9901079.

[10] S. K. Bogner, R. J. Furnstahl, and R. J. Perry, "Similarity renormalization group for nucleon-nucleon interactions," *Phys. Rev.*, vol. C75, p. 061001, 2007.

[11] R. Roth, H. Hergert, P. Papakonstantinou, T. Neff, and H. Feldmeier, "Matrix elements and few-body calculations within the unitary correlation operator method," *Phys. Rev.*, vol. C72, p. 034002, 2005.

[12] R. Roth, "Theoretische Kernphysik." Vorlesungsskript, WS 2006/2007.

[13] H. Feldmeier, "Theoretische Kernphysik." Vorlesungsskript, WS 2007/2008.

[14] J. Chadwick, "The existence of a neutron," *Proc. Roy. Soc.*, vol. A 136, pp. 692–708, 1932.

[15] D. Iwanenko, "The neutron hypothesis," *Nature*, vol. 129, p. 798, 1932.

[16] H. Yukawa, "On the interaction of elementary particles," *Proc. Phys. Math. Soc. Jap.*, vol. 17, p. 48, 1935.

[17] S. C. Pieper, V. R. Pandharipande, R. B. Wiringa, and J. Carlson, "Realistic models of pion-exchange three-nucleon interactions," *Physical Review C*, vol. 64, p. 014001.

[18] S. Weinberg, "Phenomenological Lagrangians," *Physica*, vol. A96, p. 327, 1979.

[19] S. Weinberg, *The Quantum Theory of Fields, Volume 2: Modern Applications*. Cambridge University Press, 2005.

[20] V. Bernard, N. Kaiser, and U.-G. Meissner, "Chiral dynamics in nucleons and nuclei," *Int. J. Mod. Phys.*, vol. E4, pp. 193–346, 1995.

[21] N. Kaiser, "Chiral 3pi exchange NN potentials: Results for representation-invariant classes of diagrams," *Phys. Rev.*, vol. C61, p. 014003, 2000.

[22] H. Hergert, "Correlated NN–interactions and phenomenological corrections for nuclear structure calculations," diploma thesis, TU Darmstadt, 2004.

[23] R. Roth, T. Neff, H. Hergert, and H. Feldmeier, "Nuclear structure based on correlated realistic nucleon- nucleon potentials," *Nucl. Phys.*, vol. A745, pp. 3–33, 2004.

[24] B. H. Bartlett, "Flow equations for hamiltonians from continuous unitary transformations," 2003.

[25] F. J. Wegner, "Flow equations for hamiltonians," *Nucl. Phys. Proc. Suppl.*, vol. 90, pp. 141–146, 2000.

[26] F. Wegner, "Flow-equations for hamiltonians," *Ann. Phys.*, 1994.

[27] S. Szpigel and R. J. Perry, "The similarity renormalization group," 2000, hep-ph/0009071.

[28] P. Navrátil and W. E. Ormand, "Ab initio shell model calculations with three-body effective interactions for p-shell nuclei," *Phys. Rev. Lett.*, vol. 88, p. 152502, Apr 2002.

[29] P. Navratil, J. P. Vary, and B. R. Barrett, "Properties of ^{12}C in the *ab initio* nuclear shell-model," *Phys. Rev. Lett.*, vol. 84, pp. 5728–5731, 2000.

[30] P. Navratil, J. P. Vary, and B. R. Barrett, "Large basis ab initio no-core shell model and its application to C-12," *Phys. Rev.*, vol. C62, p. 054311, 2000.

[31] P. Navratil and B. R. Barrett, "No-core shell-model calculations with starting- energy-independent multi-valued effective interactions," *Phys. Rev.*, vol. C54, pp. 2986–2995, 1996.

[32] S. K. Bogner, R. J. Furnstahl, P. Maris, R. J. Perry, A. Schwenk, and J. P. Vary, "Convergence in the no-core shell model with low-momentum two-nucleon interactions," 2007.

[33] K. Heyde, *Basic ideas and concepts in nuclear physics*. Institute of Physics Publishing, second ed., 1999.

[34] R. Roth *et al.*, "Hartree-Fock and many-body perturbation theory with correlated realistic nn-interactions," *Phys. Rev.*, vol. C73, p. 044312, 2006.

[35] A. Zapp, "Kernstruktur mit effektiven Dreiteilchenpotentialen," diploma thesis, TU Darmstadt, 2006.

[36] C. Barbieri, N. Paar, R. Roth, and P. Papakonstantinou, "Correlation energies in the random phase approximation using realistic interactions," 2006, nucl-th/0608011.

Danksagung

Zuerst möchte ich mich bei Prof. Robert Roth bedanken für die Möglichkeit diese Arbeit anzufertigen. Seine motivierende Art und sein anhaltendes Interesse haben zum Gelingen erheblich beigetragen.
Heiko Hergert danke ich für die Beantwortung meiner Fragen und das Korrekturlesen dieser Arbeit.
Ein weiterer Dank gebührt Hannes Basler und Jens Müller für die spannenden Diskussionen über physikalische und nicht-physikalische Themen. Hannes Basler danke ich ausserdem für seine Hilfe bei den lästigen Computerproblemen.
Bei den Mitgliedern der Theorieabteilung des Instituts für Kernphysik möchte ich mich für die freundliche Aufnahme und die vielen Kuchen bedanken.
Den Jungs aus dem *Kinderzimmer* danke ich für die interessanten Diskussionen und die lustigen Teerunden.
Meiner Familie danke ich für die Unterstützung ohne die ein Studium nicht möglich gewesen wäre.
Meinen Freunden danke ich für die Ablenkung und die vielen kulinarischen Höhepunkte.
Bei Lars bedanke ich mich für seine Liebe und Unterstützung auch wenn es mal nicht so einfach war.

Erklärung gemäß §19 Abs.6 DPO

Hiermit versichere ich, die Diplomarbeit ohne Hilfe Dritter nur mit den angegeben Quellen und Hilfsmitteln angefertigt zu haben. Alle Stellen, die Quellen entnommen wurden, sind als solche gekennzeichnet. Diese Arbeit hat in gleicher oder ähnlicher Form noch keiner Prüfungsbehörde vorgelegen.